Doppler Weather Radar

RICHARD J. DOVIAK, SENIOR MEMBER, IEEE, DUSAN S. ZRNIĆ, SENIOR MEMBER, IEEE, AND DALE S. SIRMANS

Abstract—The Doppler weather radar and its signals are examined from elementary considerations to show the origin and development of useful weather echo properties such as signal-to-noise ratio (SNR), range correlation, signal statistics, etc. We present a form of the weather radar equation which explicitly shows the echo power loss due to finite receiver bandwidth and how it is related to the range weighting function. Echoes at adjacent range samples have a correlation that depends on receiver bandwidth-transmitter pulsewidth product as well as sample spacing. Stochastic Bragg scatter from clouds is examined, but experimental work is required to determine if this echo power is larger than incoherently scattered power. Section III presents the relation between Doppler power spectrum and the distribution of reflectivity and velocity within a resolution volume. A new formula that relates spectrum width to the shear of radial velocities as well as turbulence, signal decorrelation from antenna rotation, and signal processing biases is presented. The estimation of power spectral moments is reviewed and properties of the most commonly used algorithms are discussed. Section V highlights some of the considerations that need to be made for Doppler radar observation of severe thunderstorms. Echo coherency is shown to limit the pulsed Doppler radar's unambiguous range and velocity measurements. Single and dual Doppler-radar techniques for wind measurements are reviewed. Observations of thunderstorms show tornado cyclones, and clear air measurements in the boundary layer reveal turbulence and waves.

NOMENCLATURE

A	prefilter amplitude
A_i	filter output amplitude of ith scatterer
$A(\vec{r})$	scatterer's weight per unit volume
B_6	receiver-filter bandwidth, 6-dB width in Hz
c	propagation speed, 3×10^8 m · s^{-1}
C_n^2	refractive index structure constant
D	diameter of the antenna system
d	separation of radars for dual radar system
$D_{\Delta n}$	structure function of refractive index
f_w	normalized range weighting function
$f^2(\theta, \phi)$	normalized one-way power gain or radiation pattern
g	maximum measured antenna gain; gravitational constant
$I(\vec{r}, \vec{r}_1)$	weighting function of resolution volume
I_0, Q_0	prefilter echo amplitude, inphase and quadrature components
$I(t), Q(t)$	inphase and quadrature phase signal at filter output
k	attenuation rate due to droplets (m^{-1}); also an integer
k_g	gaseous attenuation rate
k_θ, k_ϕ, k_r	shear along θ, ϕ, and r directions
K	wavenumber $= 2\pi/\Lambda$
$\lvert K\rvert^2$	a parameter proportional to raindrop's refractive index
l	one-way propagation loss due to scatter and absorption
l_r	echo power loss due to finite bandwidth receiver
M	number of echo samples along sample-time axis; mean molecular weight
n	integer; also refractive index
N	thermal noise power
N_s	number of scatterers
$P(\vec{r})$	echo power of resolution volume centered at $\vec{r}$
P_t	power delivered to the antenna system
PRT	pulse repetition time
P_r	point target echo power at the antenna port
$P(\tau_s)$	instantaneous weather echo power (W)
$\bar{P}(\tau_s)$	mean weather echo power at sample time-range delay τ_s
Q	output of radar receiver
$r_{1,2}$	range from radar 1, 2 to grid point
r	range from source to target or resolution volume location
r_a	unambiguous range $cT_s/2$
r_6	6-dB range width of resolution volume
$R(\vec{\rho})$	spatial covariance of $A(\vec{r})$
$R(T_l)$	autocovariance at lag T_l
R_{vv}	correlation of samples spaced along range time
$S(f)$	power spectrum in frequency domain
S	expected echo sample power
$\bar{S}(r, v)$	power spectrum in velocity domain for resolution volume center at r
$\bar{S}_n(r, v)$	normalized power spectrum
SNR	signal-to-noise ratio
T	air temperature (K)
T_l	time lag
T_s	pulse repetition time (PRT) or sample time interval
T_d	dwell time to resolve target location in FM-CW radar
$U(t)$	mathematical symbol representing a pulse: $U = 1$ when $0 \leqslant t \leqslant \tau$; otherwise it is zero
$v(\vec{r}_1)$	radial velocity field at a point
v_a	Nyquist velocity $\lambda/4T_s$
$v_{1,2}$	mean Doppler velocities corrected for target fall-speed at data points for radars 1, 2
$\hat{v}_{pp}$	pulse pair estimate of Doppler velocity
$\bar{v}_{1,2}$	mean Doppler velocity at a grid point
$v'_{1,2}$	mean Doppler target velocities measured by radars 1, 2
v_t	mean terminal velocity of drops in resolution volume
v_h	horizontal wind speed

Manuscript received November 28, 1978; revised July 30, 1979. This work was partially supported by the FAA under Contract DOT/FA76 WAI-622 (RC360205), the NWS under Contract 8AA80901, the NRC under Contract RC370503, and the ERDA under Contract RD840520. The submission of this paper was encouraged after review of an advance proposal.

The authors are with the National Severe Storms Laboratory, NOAA, Norman, OK 73069.

0018-9219/79/1100-1522$00.75

v_r	radial component of velocity (Doppler velocity)
$V_0(t)$	prefilter receiver output voltage
$V(t)$	echo signal voltage
$V(\tau_s)$	weather echo voltage sample at $\tau = \tau_s$
V_s	resolution volume
$V(nT_s)$	echo samples along sample-time axis
w_ρ, w_s, w_α	cylindrical wind components
w_z	vertical wind speed
w	vertical velocity of tracers
$W(r_i)$	ith scatterer range weight due to receiver filter
Z	reflectivity factor
α	angular coordinate; antenna rotation rate; rate of frequency change in an FM-CW radar
γ	air density; phase
δ	wind direction
$\delta\tau_s$	range-time sample spacing
Δr	range over which samples are averaged
θ_2	two-way half-power beamwidth
η	target reflectivity cross section per unit volume (m^{-1})
θ_s	angle between incident and scatter direction
θ_1	beamwidth between half-power points of one way antenna pattern
θ, ϕ	radar beam elevation and azimuth angles in horizon coordinates ($\phi = 0$ at true north); also angular position of scatterer relative to beam axis
λ	radar wavelength (m)
λ_s	structure wavelength
Λ	wavelength of wind fluctuations
ρ	perpendicular distance from axis of cylindrical coordinate system
σ_b	backscatter cross section
$\sigma_d, \sigma_r, \sigma_s, \sigma_t$	spectrum width due to drop fall speed differences, antenna rotation, shear, and turbulence
σ_v	total spectrum width of Doppler spectrum
σ^2	mean square value of I or Q
$\sigma_{s\theta}, \sigma_{s\phi}, \sigma_{sr}$	spectrum widths contributed by shear along θ, ϕ, and r, respectively
$\sigma_\theta^2, \sigma_\phi^2$	second moment of the two-way antenna pattern
σ_r^2	second moment of the range weighting function
τ	pulsewidth
τ_s	time delay between transmitted pulse and the echo sample.

I. Introduction

RADARS were developed to detect and determine the range of aircraft by radio techniques, but as they became more powerful, their beams more directive, receivers more sensitive, and transmitters coherent, they also found highly successful applications in mapping the earth's surface and atmosphere, and their signals have reached out into space to explore surface features on our planetary neighbors. Recently pulsed Doppler radar techniques have been applied to map severe storm reflectivity and velocity structure with some astounding success, particularly showing, in real time, the development of incipient tornado cyclones [24], [42], [45]. The radar beam penetrates thunderstorms and clouds to reveal the dynamical structure inside of an otherwise unobservable event. This inside look will help researchers understand the life cycle and dynamics of storms. The first detection of storms by microwave radar was made in England in early 1941. An excellent historical review of the early developments in radar meteorology can be found in Atlas' work [5]. A more recent article appeared in the PROCEEDINGS [113].

Because the angular resolution $\Delta\theta$ in degrees (°) at wavelength λ is well approximated by $\Delta\theta \simeq 70\ \lambda/D$ where D is the diameter of the antenna system [16], it is evident that remote radio sensing, even at microwave frequencies, is characterized by poor spatial resolution compared to optical standards. One essential distinguishing feature favoring microwaves is its property to *see* inside rain showers and thunderstorms, day or night. Rain and cloud do attenuate microwave signals, but slightly (for $\lambda > 0.05$ m) compared to the almost complete extinction of optical signals. Scattered signal strength can be related to rain intensity, and time rate of change of phase (Doppler shift) is a measure of raindrop radial speed.

Development of high power and high gain klystron amplifiers in the 1950's made practical the generation of microwaves that are phase coherent pulse to pulse, a requirement for pulsed Doppler radars if velocities of other than first time around (first trip) echoes are to be measured [89]. Radar signals are phase coherent from pulse to pulse if the distance (or time) between wave crests of successive transmitted pulses is fixed or known. Magnetron oscillators, phase incoherent pulse to pulse, can only be used for Doppler measurements of targets beyond the first trip if provision is made to store phase for time durations longer than the pulse repetition time (PRT).

The first reported use of a Doppler radar to observed weather was made by Brantley and Barczys in 1957 [19]. A rapid development of Doppler techniques followed. Boyenval [17] deduced the drop size distribution of Rayleigh scatterers from the Doppler spectrum while Probert-Jones and Harper [96] used vertically pointed antenna and storm motion to produce a vertical cross section [10]. Zenith-pointing Doppler radars can be used to estimate vertical air velocities as a function of height and time, can yield data from which one can sometimes infer the nature of the hydrometeors (snow, rain, or hail), and in some instances, yield data for calculating hydrometeor size distributions [11].

These earliest observations of radial velocities used analog spectrum analyzers or filter banks that have economical utility for, at most, observations in a few resolution volumes. Atlas [4] recognized the utility of scanning storms horizontally to map radial velocities on a plan-position indicator (PPI) type display and Lhermitte [81] accurately assessed requirements for the development of a viable pulsed Doppler radar. These early investigators foresaw real-time severe storm and tornado warnings from pulsed Doppler observations of storm circulations and their predictions were to be verified a few years later by several investigating teams [24], [25], [42], [45]. The first remote measurement of tornadic wind speed was accomplished in 1958 by Smith and Holmes [112] using a 3-cm continuous wave (CW) Doppler radar.

Real-time reflectivities displayed on PPI have been available to radar meteorologists since the mid-1940's. The PPI shows reflectivity distributions on conical surfaces as the antenna beam sweeps in azimuth at constant elevation angle. But real-time Doppler velocity mapping was a goal that eluded researchers until the late 1960's.

Contrary to reflectivity estimation which only requires echo sample averaging to reduce statistical fluctuations, mean velocity estimation requires sophisticated data processing. Probably the long development and cost of Doppler processors (to estimate velocities simultaneously at all resolution volumes along the beam) lay principally in preoccupation with pursuit of

spectrum measurements, from which the most interesting moments (mean velocity and spectrum width) need to be extracted.

One of the first Doppler spectrum analyzers that could indeed generate velocity spectra in real time for each contiguous resolution volume is described by Chimera [33], and this machine, called a velocity indicating coherent integrator, processed with a single electronic circuit the echo signals to generate spectrum estimates simultaneously at all resolution volumes. Another machine, called the coherent memory filter (CMF), employing the same principles was developed [62] for weather radar observations and used by researchers at the Air Force Cambridge Research Laboratories (AFCRL).[1] This machine produced the first real-time maps of velocity fields on a PPI [3].

In the early seventies Sirmans and Doviak [108] described a device that generates digital estimates of mean Doppler velocity of weather targets. This device, a phase change estimator, circumvented spectral calculations and digitally processes echoes in contiguous resolution cells at the radar data rate.

The need to obtain the principal moments economically and with minimum variance, and have these in digital format (to facilitate processing and analysis with electronic computers) has led researchers to use covariance estimate techniques popularly known as pulse pair processing described in Section V. Hyde and Perry reported an early version of this method [72], but it was first used by ionosphere investigators at Jicamarca [123]. Independently and at about the same time Rummler [102], [103] introduced it to the engineering community. Soon the advantages of *pulse pair* (PP) processing became evident, and scientists at several universities and government laboratories began implementing this signal processing technique on the Doppler weather radar [83], [88], [91], [110].

A single Doppler radar maps a field of radial velocities. Two such radars spaced apart to view the winds nearly orthogonally can be utilized to reconstruct the two-dimensional wind field in the planes containing the radials [2], [82]. With help of the air mass continuity equation the third wind component can be estimated and thus the total three-dimensional wind field within the storm may be reconstructed. This is most significant as it will enable one to follow the kinematics during birth, growth, and dissipation of severe storms and thus perhaps understand storm initiation and evolution. It may even provide the answer as to why some storms reach great severity while others under *similar* conditions do not.

Doppler radars are not limited to the study of precipitation laden air. The kinematic structure of the planetary boundary layer (PBL) has been mapped even when particulate matter does not offer significant reflectivity [47]. Coherent processing can often improve the detection of weather echoes [67]. Measurement at VHF [60] and UHF [9], [36] suggests height continuous clear air returns to over 20 km, and experiments with a moderately powerful radar at S band consistently show reflectivity in the first kilometer or two [30].

Although the Doppler radar became a valuable tool in meteorological research, it has not yet been transferred to routine operational applications. As a matter of fact, several government organizations (The National Weather Service, Air Weather Service, Air Force Geophysical Laboratory, Federal Aviation Administration and the National Severe Storms Laboratory) are presently engaged in a joint experiment, the purpose of which is to demonstrate the utility of the Doppler radar for severe storm warnings and establish guidelines for the design of next generation weather radars [25]. We anticipate that the new radars with Doppler capability will go in production in the 1980's and believe that this paper will acquaint the electrical engineering community with some specifics of Doppler weather radar, weather echo data processing, and meteorological interpretation.

[1] Presently the Air Force Geophysics Laboratory.

II. The Doppler Weather Radar and Its Signals

Fig. 1 shows in a simplified block diagram the principal components of a pulsed Doppler radar. The klystron amplifier, turned on and off by the pulse modulator, transmits a train of high "peak" power microwave pulses having duration τ of about 1 μs with spacing at the PRT designated as T_s, the sampling time interval. The antenna reflector, usually a parabola of revolution, has a tapered illumination in order to reduce sidelobe levels. Weather radars measure a wide range of volumetric target cross sections; the weakest (about 10^{-17} m^2/m^3) associates with scatter from the aerosol-free troposphere, the strongest with cross sections (3×10^{-5} m^{-1}) of heavy rain. Needless to say, antenna sidelobes place limitations on the weather radar's dynamic range and can lead to misinterpretation of thunderstorm heights [41] and radial velocity measurements [122].

The backscatter cross section σ_b of a water drop with a diameter D_i small compared to λ (Rayleigh approximation, i.e., $D_i \leqslant \lambda/16$) is

$$\sigma_b = \frac{\pi^5}{\lambda^4} |K|^2 D_i^6 \tag{2.1}$$

where $|K|^2$ is a parameter, related to the refractive index of the water, that varies between 0.91 and 0.93 for wavelengths between 0.01 and 0.10 m and is practically independent of temperature [11, p. 38]. Ice spheres have $|K|^2$ values of about 0.18 (for a density 0.917 g/cm^3) which is independent of temperature as well as wavelength in the microwave region. There is an abundance of experimental and theoretical work that relates particle cross section to its shape, size relative to wavelength when $D_i \geqslant \lambda/16$, temperature, and mixture of phases (e.g., water-coated ice spheres). These works are well reviewed by Battan [11] and Atlas [5].

Were it not for electromagnetic energy absorption by water or ice drops, radars with shorter wavelength radiation would be much more in use because of the superior spatial resolution. Short wavelength (e.g., λ = 3 cm) radars suffer echo power loss that can be 100 times larger than radars operated with $\lambda \geqslant 10$ cm [12]. Weather radar meteorologists are not only interested in the detection of weather but also need to make quantitative measurement of target cross section in order to estimate rainfall rate. Thus it is important to consider losses that are greater than a few tenths of a decibel.

Besides attenuation due to rain and cloud droplets, there is attenuation due to energy absorbed by the atmosphere's molecular constituents, mainly water vapor and oxygen. This gaseous attenuation rate k_g is not negligible if accurate cross section measurements are to be made even at λ = 10 cm when storms are far away ($r \geqslant 60$ km) and beam elevation is low ($\theta_0 \leqslant 2°$) [15].

The above considerations lead to the radar equation for a single hydrometeor having backscatter cross section σ_b, and

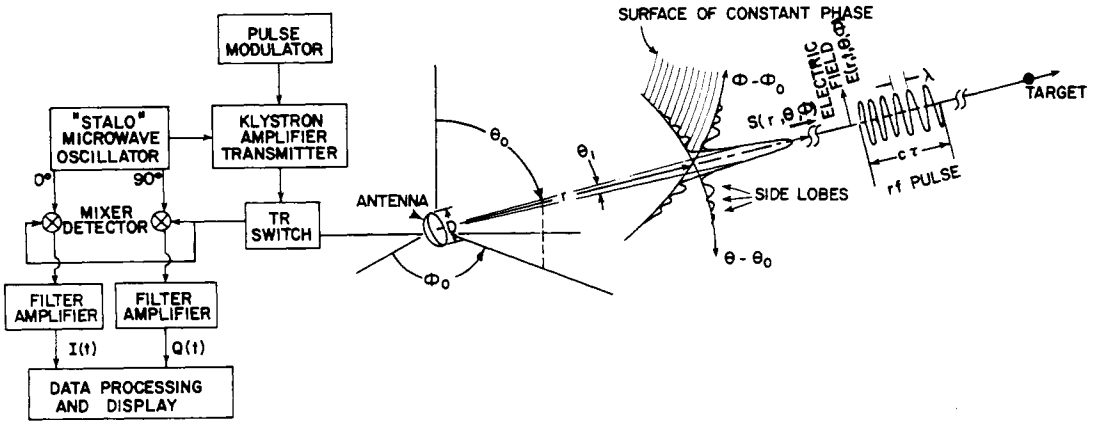

Fig. 1. Simplified Doppler radar block diagram.

located at angles (θ, ϕ) from the antenna axis

$$P_r = \frac{P_t g^2 \lambda^2 l^2 \sigma_b f^4(\theta, \phi)}{(4\pi)^3 r^4} \tag{2.2}$$

where P_t is the power delivered to the antenna port, g the maximum measured gain, $f^2(\theta, \phi)$ the normalized radiation function, and $l = \exp -[\int (k_g + k)\, dr]$ the one-way loss factor due to gaseous k_g and droplet k (both cloud and precipitation) attenuation. The measured gain, a ratio of far-field power density $S(\theta, \phi)$ to the density if power was radiated isotropically, accounts for losses associated with the antenna system (e.g., radome, waveguide, etc.).

A. The Doppler-Echo Waveform (Inphase and Quadrature Components)

When there is a single discrete target, the echo signal voltage $V(t)$ replicating the transmitted electric field waveform E is proportional to it;

$$V(t, r) = A \exp [j2\pi f(t - 2r/c) + j\psi]\, U(t - 2r/c) \tag{2.3}$$

where $2r$ is the total path traversed by the incident and scattered waves, A the prefilter echo amplitude, c velocity of light, and $U = 1$ when its argument is between 0 and τ, otherwise it is zero. After detection and filtering (to remove the carrier frequency f and harmonics generated in the detection process), we obtain a signal

$$V_0(t, r) = \underbrace{bA \exp \left[-j\left(\frac{4\pi r}{\lambda} - \psi\right)\right] U(t - 2r/c)}_{\text{modulating signal}} \underbrace{\exp (j2\pi f_\Delta t)}_{\text{difference frequency signal}} \tag{2.4}$$

if receiver bandwidth is sufficiently large. Thus heterodyning and detection serve only to shift the carrier frequency without affecting the modulation envelope (for simplicity Fig. 1 shows homodyning wherein STALO frequency is the same as the transmitted frequency, i.e., $f_\Delta \equiv 0$). A Doppler radar usually has two mixers in order to resolve the sign of the Doppler shift; in one the STALO signal is phase shifted by 90° prior to mixing so that the detected and filtered output of this mixer is equal to (2.4) but phase shifted by $\pi/2$. The actual signal from the mixer is the real part of (2.4) and for the homodyne receiver (or after a 2nd mixing step to bring f_Δ to zero) the two mixer outputs are

$$I_0(t, r) = \frac{A}{\sqrt{2}} U(t - 2r/c) \cos \left(\frac{4\pi r}{\lambda} - \psi\right) \tag{2.5a}$$

$$Q_0(t, r) = \frac{-A}{\sqrt{2}} U(t - 2r/c) \sin \left(\frac{4\pi r}{\lambda} - \psi\right) \tag{2.5b}$$

the inphase $I_0(t)$ and quadrature $Q_0(t)$ components of the modulating signal. For convenience we ignored losses (i.e., set $b = 1$) and used a $\sqrt{2}$ factor in (2.5) so that the sum of average power in I and Q channels equals input power $A^2/2$ averaged over a cycle of the microwave signal.

If r increases with time, the phase $\gamma = -4\pi r/\lambda + \psi$ decreases and the time rate of phase change

$$\frac{d\gamma}{dt} = -\frac{4\pi}{\lambda}\frac{dr}{dt} = -\frac{4\pi}{\lambda} v_r = \omega_d \tag{2.6}$$

is the Doppler shfit. It is relatively easy to see from (2.6) that, for usual radar conditions (i.e., $\tau \approx 10^{-6}$ s and weather target velocities of the order of tens of m · s^{-1}, the change in signal phase is extremely small during the modulating envelope $U(t - 2r/c)$. Thus we measure target phaseshift over a time, $T_s \approx 10^{-3}$ s from echo to echo rather than during a pulse period. Because of this the pulse Doppler radar behaves as a phase sampling device; samples are at $t = \tau_s + (n - 1)T_s$ where τ_s is the time delay between the nth transmitted pulse and its echo, and is denoted as *range time* because it is proportional to range (i.e., $\tau_s = 2r/c$).

It is convenient to introduce another time scale, designated *sample time*, wherein time is incremented in discrete T_s steps after $t = \tau_s$. Echo phase and amplitude changes are usually examined in sample-time space at the discrete instants $(n - 1)T_s$ for a target at range time τ_s. However, there have been efforts to measure phase change within a time τ in order to eliminate aliasing problems that plague observations of storm systems [50].

The receiver's filter (Fig. 1) response is usually a monotonically decreasing function of frequency and its width B_6 is best specified as the frequencies within which the response is larger than one-fourth of its highest level—its 6-dB width [119]. The larger is B_6, the better is the fidelity of the echo pulse shape, but noise power increases in proportion to B_6. Bandwidths can be adjusted to optimize signal detection performance [134], but optimization causes receiver bandwidth loss that should be part of the weather radar equation [90]. Fur-

thermore, filter response is associated with a spatial weight along the range-time axis whose form is just as important to the radar meteorologist as the antenna pattern weight is along angular directions. We consider these in the weather radar equation (Section II-C).

B. Weather Echo Samples

Weather echoes are composites of signals from a dense array of hydrometeors, each of which can be considered a point target. In this section we show the origin of the statistical properties of the echo samples $V(\tau_s)$ and instantaneous power $P(\tau_s)$ and discuss incoherent, coherent, and Bragg scatter. The echo voltage sample $V(\tau_s)$ is a composite

$$V(\tau_s) = \sum_i A_i \exp(j4\pi r_i/\lambda) \tag{2.7}$$

of discrete echoes from all the scatterers, each of which has a weight A_i determined by the scatterer's cross section σ_b, the radiation pattern $f^4(\theta, \phi)$, and receiver bandwidth–transmitted pulsewidth product $B_6\tau$. These latter weighting functions determine a resolution volume in space wherein targets significantly contribute to the echo sample at τ_s. The echo sample power averaged over an r - f cycle is proportional to

$$P(\tau_s) \propto \frac{1}{2}[VV^*] = \frac{1}{2}\sum_{i,k}^{N_s} A_i A_k^* \exp[j4\pi(r_i - r_k)/\lambda]$$

$$\propto \frac{1}{2}\sum_i A_i^2 + \frac{1}{2}\sum_{i\neq k}^{N_s} A_i A_k^* \exp[j4\pi(r_i - r_k)/\lambda]. \tag{2.8}$$

The above is the instantaneous echo power $P(\tau_s)$ for one transmission and N_s is the number of scatterers. If scatterers within a resolution volume move randomly a significant fraction of a wavelength (e.g., $\lambda/4$) between successive transmissions, each successive echo sample $V(\tau_s)$ (spaced T_s) will be essentially uncorrelated. In order to make measurements of the scatterer's mean radial speed, the time T_s between successive samples must be small so that contiguous echoes, at fixed delay τ_s, are correlated.

The first sum in (2.8) is a constant independent of scatterer's position and is portional to the zeroth moment of the Doppler spectrum, whereas the second represents the fluctuating portion of the instantaneous power and contains the Doppler velocity information. Although the second sum can be significantly larger than the first (it has $N_s(N_s - 1)$) contributions compared to N_s for the first term) for some echo samples, its average over many successive samples (i.e., sample-time average) approaches zero for spatially uniform distributions because the sample-time average of the exponential term tends to zero. The first sum is then the mean power $\bar{P}(\tau_s)$. An accurate estimate of this term is important because it relates to the meteorological estimates of liquid water in the resolution volume.

1) Incoherent and Bragg Scatter: Because radar meteorologists relate echo power to the first term in (2.8), it is important to be aware of the conditions under which the sample-time average of the 2nd term is negligible. The first term represents incoherent scatter because its power is proportional to the number of scatterers; the time average of the second term represents coherent scatter [106]. If scatterers are not independent, but have their positions correlated, we then have a statistically varying nonuniform scatterer density. In this case it is possible to have the 2nd term of (2.8) give a time average larger than the first! We estimate it in the following way.

Consider a density function $A(\vec{r})$ that describes the scatterer's weight per unit volume. Then analogous to (2.7)

$$V(\tau_s) = \int_{V_s} A(\vec{r}) \exp(j4\pi r/\lambda)\, dV_s \tag{2.9}$$

which is the Fourier composition of $A(\vec{r})$ along the radial direction (for bistatic radars the composition is analyzed along the mirror direction). Hence the intensity of the scattered signal depends directly upon the Fourier content of the scatterer's cross section per unit volume [118]. V_s is the volume over which $A(\vec{r})$ contributes significantly to $V(\tau_s)$–e.g., the resolution volume: see Section II-C1.

When $A(\vec{r})$ is an random function and can only be described in a statistical way, it can be shown that the sample-time average of $P(\tau_s)$ is

$$\bar{P}(\tau_s) = \frac{V_s}{2}\int \exp(-j4\pi\rho/\lambda) R(\vec{\rho})\, dV_s + \frac{1}{2}\left|\int \overline{A(\vec{r})} \cdot \exp(j4\pi r/\lambda)\, dV_s\right|^2 \tag{2.10a}$$

where

$$R(\vec{\rho}) \equiv \overline{[A(\vec{r}) - \bar{A}(\vec{r})][A^*(\vec{r}') - \bar{A}^*(\vec{r}')]} \tag{2.10b}$$

is the spatial covariance of $A(\vec{r})$ for a statistically homogeneous medium, $\vec{\rho} \equiv \vec{r} - \vec{r}'$, and the overbar is a sample-time average. To arrive at (2.10) we assumed that the resolution volume size is large compared to the scales over which $R(\vec{\rho})$ has significant value. The first term in (2.10a) is due to fluctuations in the density of scatterers while the second term is steady and comes from the mean structure of the density (i.e., specular scattering). If particle positions are uncorrelated, $R(\vec{\rho})$ is a Dirac delta function having a weight so that the first term in (2.10a) is equal to incoherent scatter [106]. If in addition $A(\vec{r})$ is constant and the radial extent of resolution volume large compared to wavelength, steady backscatter from the mean structure is negligible.

Scatter in any direction comes from Fourier components having a structure wavelength λ_s related to radio wavelength

$$\lambda_s = \lambda/2 \sin(\theta_s/2) \quad \text{(Bragg's Law)} \tag{2.11}$$

where θ_s is the angle between the incident and scattered-wave directions ($\theta_s = \pi$ for monostatic radar). While it is customary to define Bragg scatter as being from a periodic structure in the mean density profile, one can define a stochastic Bragg scatter if it arises from the shape of the correlation function. Thus the first term in (2.10a) contains the incoherent scatter and stochastic Bragg scatter. Chernikov [31] has determined the relative strengths of Bragg and incoherent scatter and related it to the spatial covariance of cloud liquid water content. He shows conditions of side scatter where stochastic Bragg scatter is much larger than incoherent scatter and hence might be important for electromagnetic interference from rain showers.

Bragg scatter is commonly ignored in studies of precipitation backscatter, but it would be significant if the liquid water's covariance function indicated scale sizes less than a few meters. Although stochastic Bragg scatter may be negligible for precipitation backscatter, it is not for echoes from clear air. Indeed clear air radar echoes are a result of Bragg scatter because $A(r)$

has fluctuations at scales equal to $\lambda/2$ although $\overline{A(\vec{r})}$ might be $\vec{r}$ independent (i.e., no steady echoes). Incoherent scatter from air molecules at microwave frequencies is usually many orders of magnitude smaller than stochastic Bragg scatter.

2) Signal Statistics: The I and Q components of the echo's sample are random variables if scatterers' positions change in an unpredictable way. Because I, Q are comprised of a large number of contributions, each of which is not a significant portion of the whole, we can invoke the central limit theorem [94, p. 266] to deduce that I and Q amplitudes have a Gaussian probability distribution with zero mean. Thus I and Q are jointly normal [94, p. 182] random variables and Davenport and Root [38, p. 160] have shown that I and Q from a narrow-band Gaussian process have zero correlations. Thus the probability distribution of I and Q is

$$\text{Prob}\,(I, Q) = \frac{1}{2\pi\sigma^2} \exp\left(-I^2/2\sigma^2 - Q^2/2\sigma^2\right) \quad (2.12)$$

where σ^2 is the mean-square value of I (equal for Q). Because $P(\tau_s) = (I^2 + Q^2)$, we see from (2.12) that instantaneous power is exponentially distributed and its mean value is $\bar{P} = 2\sigma^2$.

C. The Weather Radar Equation

We can now relate the sample-time averaging of echo power $P(\tau_s)$ to the radar parameters and target cross section. The contribution to average echo power at the filter output from each scatterer is

$$P_i = \frac{1}{2} A_i^2 \quad (2.13)$$

which can be directly expressed in terms of radar parameters and target cross section through use of (2.2). Thus the sample-time average power at range-time delay τ_s is

$$\bar{P}(\tau_s) = \frac{P_t g^2 \lambda^2}{(4\pi)^3} \sum_i \frac{l_i^2 \sigma_{bi} f^4(\theta_i, \phi_i) W^2(r_i)}{r_i^4} \quad (2.14)$$

where $W(r_i)$ is a range weight determined by the filter bandwidth and transmitted pulsewidth.

We now consider an elemental volume ΔV that contains many scatterers. The summation of σ_{bi} over this volume normalized to ΔV defines the *target reflectivity* η

$$\eta = \lim_{\Delta V \to 0} (\Delta V)^{-1} \sum_{\Delta V} \sigma_{bi}. \quad (2.15)$$

Replacing the sum by an integration because particles are assumed closely spaced compared to the scale of the weighting functions we have the following form for the weather radar equation

$$\bar{P}(\tau_s) = \frac{P_t g^2 \lambda^2 l^2 \eta}{(4\pi)^3 r_0^2} \int_0^\infty W^2(r)\, dr \int_0^\pi \int_0^{2\pi} f^4(\theta, \phi) \sin\theta\, d\theta\, d\phi. \quad (2.16)$$

In the above it is assumed $f^4(\theta, \phi) W^2(r)$ has a scale (resolution volume dimensions) such that the reflectivity and attenuation can be considered constant over the region which contributes most to $\bar{P}(\tau_s)$. Range r_0 is the distance at which $W^2(r)$ is maximum and is assumed much larger than the extent over which $W^2(r)$ has significant weight. When antenna patterns are circularly symmetric and with Gaussian shape, it can be shown [95] that

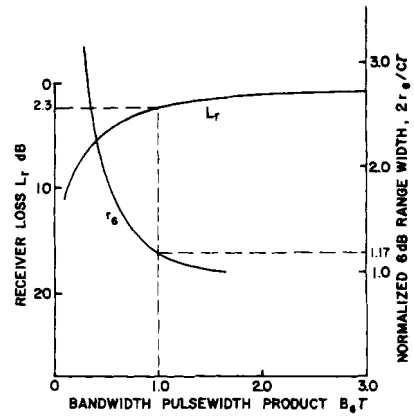

Fig. 2. Receiver signal power loss L_r (dB) and normalized 6-dB range width, $2r_6/c\tau$, of the resolution volume versus receiver bandwidth-pulsewidth product. Receiver frequency transfer is Gaussian and echo pulse rectangular.

$$\int_0^\pi \int_0^{2\pi} f^4(\theta, \phi) \sin\theta\, d\theta\, d\phi = \frac{\pi\theta_1^2}{8 \ln 2} \quad (2.17)$$

where θ_1 is the 3-dB width (in radians) of the one-way pattern. The range weighting function $W(r)$ can be expressed as a product of a receiver loss factor l_0 and a weighting function $f_w(r)$ whose peak is normalized to unity in order to have a form analogous to the product of gain squared g^2 and pattern function $f^4(\theta, \phi)$. That is

$$\int_0^\infty W^2(r)\, dr = \int_0^\infty l_0^2 f_w^2(\tau_s, r)\, dr \equiv \frac{l_r c\tau}{2} \quad (2.18)$$

where l_r is the echo power loss due to finite receiver bandwidth.

When the receiver has a Gaussian frequency transfer and the transmitted pulse is rectangular, $f_w(\tau_s, r)$ contains error functions [49]. The numerical integration of (2.18) with these functions, defined by Abramowitz and Stegun [1], gives a $L_r = -10 \log l_r$ dependence on the $B_6\tau$ product shown in Fig. 2. Nathanson and Smith [90] examined the exactly matched filter receiver (i.e., a $\sin x/x$ filter frequency transfer for a rectangular pulse) and deduced l_r to be 1.8 dB. We have assumed a Gaussian receiver frequency transfer characteristic and rectangular pulse shape. These two chosen characteristics often approximate those met in practice. For condition $B_6\tau = 1$ corresponding to a practical *matched* filter, the numerical integration of the function $W^2(r)$, shows $L_r \simeq 2.3$ dB, or about 0.5 dB more than that obtained with a filter transfer perfectly matched to the rectangular pulse. Thus a practical form of the weather radar equation is

$$\bar{P}(\tau_s) = \frac{P_t g^2 \lambda^2 l^2 \eta l_r \pi\theta_1^2}{(4\pi)^3 r^2 8 \ln 2} \frac{c\tau}{2} \quad (2.19)$$

where henceforth r is to be used in place of r_0. This extended form of the weather radar equation shows not only the dependency of echo power upon commonly used radar parameters, but also its relation to receiver bandwidth. Furthermore, in the limit of $B_6\tau \gg 1$, $l_r \to 1$ (see Fig. 2) so (2.19) is in agreement with the Probert-Jones radar equation [95] used widely by radar meteorologists.

1) The Resolution Volume: The 6-dB width of $f^4(\theta, \phi)$ (the two-way antenna pattern function) is taken to represent the angular width θ_1 of the resolution volume V_s. In an analogous manner we define the 6-dB width of f_w^2 to represent the range resolution r_6 of V_s. The range width r_6 versus $B_6\tau$ is also shown in Fig. 2.

2) Reflectivity Factor: Radar meteorologists need to relate reflectivity η, general radar terminology for the scatter cross section density, to factors that have meteorological significance. If scattering particles are know to be spherical and have diameters small compared to wavelength (i.e., the Rayleigh approximation), then we can substitute (2.1) into (2.15) to obtain the relation

$$\eta = \frac{\pi^5}{\lambda^4} |K|^2 Z \tag{2.20}$$

where

$$Z \equiv \frac{1}{\Delta V} \sum_i D_i^6 \tag{2.21}$$

is the "reflectivity factor." Either η or Z can be used in the radar equation, but radar meteorologists have opted for Z. When backscattering cross section can not be simply related to size, e.g., scatterers having large (compared to wavelength) diameters, or liquid–ice mixes, equation (2.20) is used to define the equivalent reflectivity factor Z_e.

The use of reflectivity factor alone really does not relate radar echo power to meteorologically significant variables such as rainfall rate or liquid water content because there is one more essential ingredient that needs to be known in addition to phase (i.e., $|K|^2$). This is the drop-size distribution. When drop size distribution is specified by two moments, Ulbrich and Atlas [120] have shown how rainfall rate and liquid water aloft are related to the remotely measurable parameters: reflectivity and attenuation.

D. Signal-to-Noise Ratio (SNR) for Weather Targets

Consistent with the previous assumptions, it can be shown that the SNR for weather targets depends upon $B_6\tau$ as [49]

$$\text{SNR} = \frac{C_0}{r^2} \frac{\tau^2 l_r}{B_6 \tau} \tag{2.22}$$

where C_0 contains constants pertaining to the radar. We immediately note that if $B_6\tau$ is a constant, then SNR is proportional to the square of the transmitted pulsewidth. It can be shown that maximum SNR is obtained as $B_6\tau \to 0$. Therefore, in *contrast* to point target measurements, we do *not* obtain a maximum of weather SNR at $B_6\tau \simeq 1$. However, even though SNR increases monotonically as B_6 decreases, resolution r_6^{-1} worsens. One can define an optimum $B_6\tau$ as that value which maximizes SNR for a given resolution. A more formal derivation leads to the following conclusion concerning weather radar design: the optimum system consists of a matched Gaussian filter and pulse which together yield the desired resolution [134].

E. Correlation of Echo Samples Along Range Time

Sample spacing along the range-time axis is usually chosen so that there are independent estimates of reflectivity and/or radial velocity along the beam. Both τ and B_6 determine the correlation of these estimates and sometimes B_6 is deliberately chosen small (i.e., not "matched" to τ) in order to observe meteorological events in a larger range interval with fewer samples along the range-time axis. This approach becomes more advantageous when real-time data processing equipment limits simultaneous observations to a few range-time samples (as is sometimes the case for real-time Doppler spectral processors) and pulsewidth cannot be increased. If B_6 is "matched" to τ or, as in many meteorological radars, large compared to τ^{-1}, then dimensionally small meteorological events such as tornadic vortices can be missed by samples spaced further than the range extent of the resolution volume or else smaller intervals will be observed causing longer time to interrogate the entire storm. When the transmitted pulse is rectangular and receiver response Gaussian, the correlation of samples along range time is shown in Fig. 3 [149]. The figure shows that when B_6 is more than twice τ^{-1}, the echo sample correlation is principally controlled by pulsewidth, whereas when B_6 is less than 0.5 τ^{-1}, it is controlled by the receiver-filter 6-dB bandwidth.

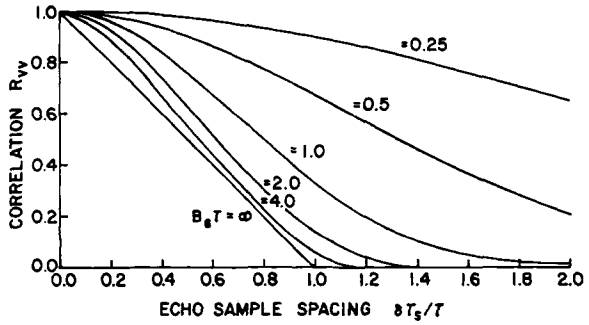

Fig. 3. Normalized correlation of echo samples spaced along the range-time axis.

III. Doppler Spectra of Weather Echoes

The Doppler spectrum is a power weighted distribution of the radial velocities of the scatterers that mostly lie within the resolution volume. Not only does the power weight depend on the reflectivity of scatterers, but it also depends on the weighting given to scatterers by the antenna pattern, the transmitted pulsewidth, and the receiver filter. A derivation leading to a relationship between the velocity and reflectivity fields, the resolution volume weighting function, and the Doppler spectrum was first put forward by Synchra [117]. Our derivation takes a somewhat different route but neverthelss leads to identical final results.

A. Power Weighted Distribution of Velocities

To begin with, we consider scatterers that produce a radial velocity field $v(\vec{r}_1)$ and a reflectivity field $\eta(\vec{r}_1)$. Let the resolution volume center be at a location $\vec{r}$ (Fig. 4) with the corresponding weighting function $I(\vec{r}, \vec{r}_1)$:

$$I(\vec{r}, \vec{r}_1) = C_1 f^4(\theta, \phi) W^2(r_1)/r_1^4 \tag{3.1}$$

where C_1 is a constant that can be obtained from (2.16); also η now has scales small compared to V_s dimensions.

We locate a surface of constant velocity $v(\vec{r}_1)$ and seek the total power contribution from scatterers in the velocity range v to $v + dv$. This contribution will obviously be a summation of powers from the volume between the two surfaces v and $v + dv$. It is convenient to choose for the elemental volume

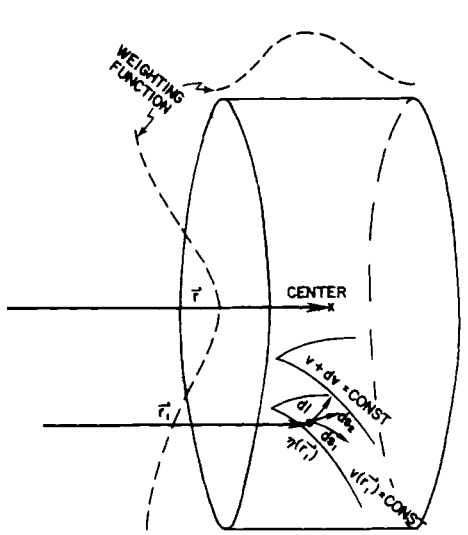

Fig. 4. Parameters and the geometry that contribute towards the weather signal power spectrum; $\eta(\vec{r}_1)$ and $v(\vec{r}_1)$ are the reflectivity and radial velocity fields, $\vec{r}$'s the center of resolution volume. The weighting functions in azimuth and range are indicated by dashes.

the product $ds_1\ ds_2\ dl$ where ds_1 and ds_2 are two orthogonal arc lengths, at a point $\vec{r}_1$, tangent to $v(\vec{r}_1) = \text{const}$ (Fig. 4).

The third coordinate dl is perpendicular to the surface of v

$$dl = |\text{grad } v(\vec{r}_1)|^{-1}\ dv. \tag{3.2}$$

The elemental volume contributes an increment of power in the velocity interval v, $v + dv$ proportional to

$$d\bar{P}(v) = \eta(\vec{r}_1)I(\vec{r}, \vec{r}_1)|\text{grad } v(\vec{r}_1)|^{-1}\ ds_1\ ds_2\ dv. \tag{3.3}$$

Finally, the integral over the surface A of constant v gives the total power in the velocity range v, $v + dv$ and is, by definition, the product of power spectrum density and dv. That is,

$$\bar{P}(v) = \bar{S}(\vec{r}, v)\ dv = \left[\iint_A \eta(\vec{r}_1)I(\vec{r}, \vec{r}_1)|\text{grad } v(\vec{r}_1)|^{-1}\ ds_1\ ds_2\right] dv. \tag{3.4}$$

The overbar in (3.4) denotes the mean (unnormalized) power spectrum.

This last equation is fundamental and is worthy of more discussion. First the area A consists of all isodop surfaces (surfaces of constant Doppler velocity) on which the radial velocity is a constant v, i.e., it is a union of such surfaces. At each point $\vec{r}_1$ on the surface the reflectivity is multiplied with the corresponding weighting function. The gradient term adjusts the isodops contribution according to their density (i.e., the closer the isodop surfaces are spaced the smaller is the weight applied to the spectral components in the velocity interval between two isodops).

So far we have considered a deterministic velocity field and a natural question to pose is how does $\bar{S}(\vec{r}, v)$ relate to the velocities of real scatterers whose relative positions change from pulse to pulse. A heuristic argument about this is as follows. Both point reflectivity $\eta(\vec{r}_1)$ and point velocity $v(\vec{r}_1)$ constantly change in time due to relative random motions of air (small scale turbulence). Equation (3.4) which was calculated for deterministic flow is valid on the average for turbulent flow as well. This simply means that if one observed under identical macroscopic conditions a statistically stationary weather phenomena and averaged the respective spectra, he would obtain, on the average, the result given in (3.4). Beware, this does not imply that a Doppler spectrum uniquely specifies the velocity and reflectivity profile in a resolution volume. On the contrary, a variety of reflectivity-velocity combinations may yield identical Doppler spectra.

For calculation of the mean velocity and the spectrum width, the normalized $\bar{S}_n(\vec{r}, v)$ version of (3.4) is used.

$$\bar{S}_n(\vec{r}, v) = \frac{\bar{S}(\vec{r}, v)}{\int_{-\infty}^{\infty} \bar{S}(\vec{r}, v)\ dv}. \tag{3.5}$$

Note that the integral in the denominator is the total power and can be obtained from the volume integral of (3.3). The sum of (3.3) throughout the volume is proportional to the weighted average reflectivity $\bar{\eta}(\vec{r})$

$$\bar{P}(\vec{r}) = \bar{\eta}(\vec{r}) \iiint I(\vec{r}, \vec{r}_1)\ dV \tag{3.6}$$

where

$$\bar{\eta}(\vec{r}) \equiv \frac{\iiint \eta(\vec{r}_1)I(\vec{r}, r_1)\ dV}{\iiint I(\vec{r}, r_1)\ dV}. \tag{3.7}$$

The integral value in the denominator of (3.7) is obtained from (2.19) for weather radar parameters usually met in practice. Now the mean Doppler velocity is defined as

$$\bar{v}(\vec{r}) = \int_{-\infty}^{\infty} v\bar{S}_n(\vec{r}, v)\ dv \tag{3.8}$$

which is a combination of reflectivity (power) and illumination function weighted velocity and could be quite different from the $I(\vec{r}, \vec{r}_1)$ weighted velocity. Likewise the velocity spectrum width $\sigma_v(r)$ is obtained from

$$\sigma_v^2(\vec{r}) = \int_{-\infty}^{\infty} [v - \bar{v}(\vec{r})]^2 \bar{S}_n(\vec{r}, v)\ dv. \tag{3.9}$$

The relationship between the point velocities $v(\vec{r}_1)$ and the power weighted moment $\bar{v}(\vec{r})$ is obtained by substituting both (3.4) and (3.5) into (3.8)

$$\bar{v}(\vec{r}) = \frac{\iiint v(\vec{r}_1)\eta(\vec{r}_1)I(\vec{r}, \vec{r}_1)\ dV}{\iiint \eta(\vec{r}_1)I(\vec{r}, \vec{r}_1)\ dV}. \tag{3.10}$$

Unlike the pulse volume averaged reflectivity, this is the average of point velocities weighted by both reflectivity and the illumination function. Similarly (3.9) reduces to

$$\sigma_v^2(\vec{r}) = \frac{\iiint v^2(\vec{r}_1)\eta(\vec{r}_1)I(\vec{r}, \vec{r}_1)\ dV}{\iiint \eta(\vec{r}_1)I(\vec{r}, \vec{r}_1)\ dV} - \bar{v}^2(\vec{r}) \tag{3.11}$$

and corresponds to a weighted deviation of velocities from the averaged velocity.

The mean velocity (3.8) depends on the distribution of scatterers cross section within the resolution volume and its

weighting functions. Thus $\bar{v}(\vec{r})$ cannot in general be equated to a spatial mean velocity. However, if wind distribution is symmetrical about the resolution volume center and reflectivity is uniform, then $\bar{v}(\vec{r})$ can be considered a very good approximation of the true radial component of wind at the volume center. But hydrometeor fall velocity must either be insignificant or known (see Section VI-A1).

A simplification of (3.4) occurs when the radial velocity field and the reflectivity are height invariant. Then the power spectrum reduces to [132]

$$\bar{S}(v,\vec{r}) = \int \left[\int_{v=\text{const}} \eta(x_1, y_1) I(\vec{r}, x_1, y_1, z_1) \cdot |\text{grad } v(x_1, y_1)|^{-1} \, ds \right] dz_1. \tag{3.12}$$

The inner integral sums the contributions along the line $s = s(x_1, y_1)$ on which $v(x_1, y_1)$ is constant. Because $ds = [dx_1^2 + dy_1^2]^{1/2}$ the integration is a surface integral with element area $ds\, dz_1$. Both $\eta(x_1, y_1)$ and $|\text{grad } v(x_1, y_1)|$ are independent of z but the illumination function may depend on it. At each point x_1, y_1 along a strip of constant v, the reflectivity is multiplied with the corresponding weighting function. To account for contributions of other infinitesimal strips within the resolution volume, integration is performed along the third (z-axis) dimension. Equation (3.12) was used to compute spectra of model tornadoes and mesocyclones. These compared well with actual measurements [132], [133] (see also Section VI-B3).

It can be shown with the help of (3.12) that when wind shear and η are constant across V_s, the power spectrum follows the weighting function shape. Because Gaussian shape approximates well the range and angular weighting patterns, we may infer, when weather spectra are Gaussian, that reflectivity and radial velocity shear are somewhat uniform within V_s.

B. Estimating Doppler Power Spectra

In order to measure the power weighted distribution of velocities, frequency analysis of $V(\tau_s)$ is needed and can be accomplished by estimating its power spectrum. It is important to bear in mind that the frequency analysis is performed along the sample-time axis for samples $V(\tau_s)$ at fixed τ_s. Thus we have discrete samples $V(nT_s)$, spaced T_s apart, of a continuous random process. Next we shall make some general statements concerning spectral analysis of continuous random signals.

The power spectrum is the Fourier transform of the signal's autocovariance function.

$$\bar{S}(f) = \int_{-\infty}^{+\infty} R(T_l) \exp(-j2\pi f T_l) \, dT_l \tag{3.13}$$

where T_l is a time lag.

The autocovariance function of a stationary (statistics do not change during the time of observation) signal is found from the time average

$$R(T_l) = \lim_{T\to\infty} \frac{1}{T} \int_{-T/2}^{T/2} V^*(t) V(t + T_l) \, dt. \tag{3.14}$$

Because $V(t)$ has zero mean, autocorrelation and autocovariance are identical [94]. Note that conservation of power relates the Doppler spectrum $S(v)$ to the power spectrum $S(f)$ via the equation

$$\bar{S}(v) = \frac{2}{\lambda} \bar{S}(f). \tag{3.15}$$

When the spectrum or the autocovariances are known, all pertinent signal parameters can be readily obtained.

Neither $\bar{S}(v)$ nor $R(T_l)$ are available; they must be estimated from the ensemble of samples $V(\tau_s)$ spaced T_s apart. Because radars observe any resolution volume for a finite time, one is faced with estimating at a given range $c\tau_s/2$ the spectrum and its parameters from a finite number M of time samples $V(nT_s)$. We shall henceforth delete the range-time argument τ_s, and $V(nT_s)$ will designate an ensemble sample at the implicit delay τ_s and T_l increments in steps of T_s.

Samples $V(nT_s)$, often multiplied by a weighting factor $W(nT_s)$, are Fourier transformed and the magnitude squared of this transformation is a power spectrum estimate $\hat{S}(k)$ commonly known as the periodogram

$$\hat{S}(k) = \frac{1}{M} \left| \sum_{n=0}^{M-1} W(nT_s) V(nT_s) \exp(-j2\pi kn/M) \right|^2 \tag{3.16}$$

where k, n are integers.

The finite number of time samples from which the periodogram is computed limits velocity resolution and creates an undesirable "window effect." Namely, one may imagine that the time series extends to infinity but is observed through a finite length window. The magnitude squared of the data window transform is referred to as the spectral window and is significant because its convolution with the true spectrum equals the measured spectrum.

An illustration of a weather signal weighted with a uniform window and one with a von Hann (raised cosine) window (Fig. 5) shows considerable difference in the spectral domain especially in spectral skirts. Since the von Hann window has a gradual transition between no data and data points, its spectral window has a less concentrated main lobe and significantly lower sidelobes. The resulting spectrum retains these properties and enables us to observe weak signals to over 40 dB below the main peak. This is very significant when one is trying to estimate the peak winds of tornadoes or other severe weather [128] within the resolution volume; power in spectral "skirts" due to high velocities is rather weak and would be masked by the strong spectral peaks seen through the sidelobes unless a suitable window is applied. The apparent lack of randomness of coefficients in the spectral skirts for the rectangularly weighted data is due to the larger correlation between coefficients. This correlation is attributed to the strong spectral powers seen through the nearly constant level window sidelobes [128].

The example on Fig. 5 is from a tornadic circulation with translation. In this case the broad spectrum results from high speed circulatory motion within the resolution volume. The envelope shape $|\sin x/x|^2$ is readily apparent for the rectangular window (at negative velocities), and the dynamic range for spectrum coefficients is about 30 dB. This is in contrast to over 45 dB of dynamic range with the von Hann window which also better defines the true spectrum and the maximum velocity (60 $\text{m} \cdot \text{s}^{-1}$). For visual clarity an estimate of the mean power from a 5-point running average is drawn on Fig. 5.

Besides the window effect which is intimately tied to signal processing, there are a number of spectral artifacts due to the

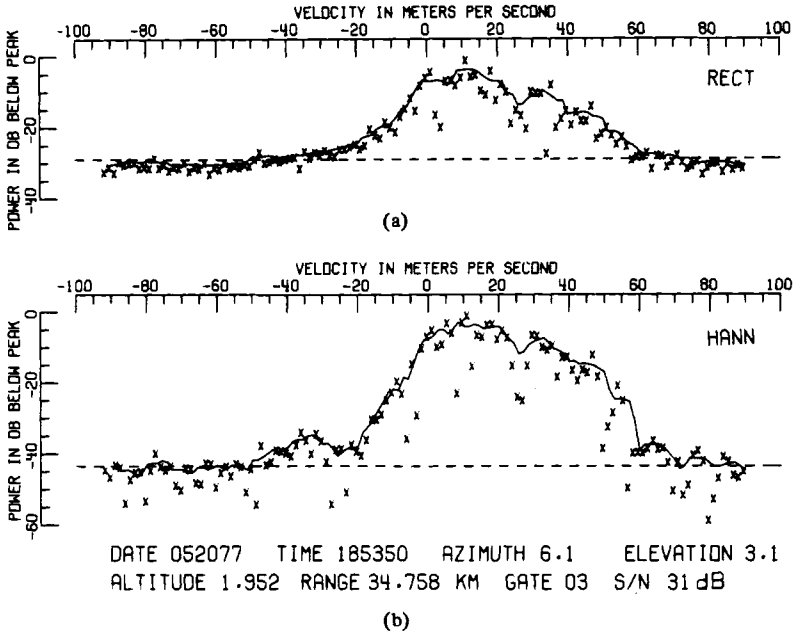

Fig. 5. Power spectra of weather echoes showing statistical fluctuations in spectral estimates denoted by x's. (a) RECT signifies spectra of echo samples unweighted whereas (b) HANN signifies samples weighted by a von Hann window. Solid curves are five point running averages of spectral powers. This spectrum is from a small tornado that touched down in Del City, OK, at 35 km from the Norman radar.

radar hardware. These are discussed in several references [126], [129], [131].

C. Velocity Spectrum Width, Shear, and Turbulence

The velocity spectrum width (i.e., the square root of the second spectral moment about the mean velocity) is a function both of radar system parameters such as beamwidth, bandwidth, pulsewidth, etc., and the meteorological parameters that describe the distribution of hydrometeor density and velocity within the resolution volume [5]. An excellent explanation and assessment of each can be found in Waldteufel's work [122]. Relative radial motion of targets broadens the spectrum. For example, turbulence produces random relative radial motion of drops. Wind shear can cause relative radial target motions as will differences in fall speeds of various size drops. There is also a contribution to spectrum width caused by the beam sweeping through space (i.e., the radar does not receive echoes from identical targets on successive samples). This change in resolution volume V_s location from pulse to pulse results in a decorrelation of echo samples and consequent increase in spectrum width σ_v. The echo samples will be uncorrelated more quickly (independent of particle motion inside V_s) the faster the antenna is rotated. Thus spectrum width increases in proportion to the antenna angular velocity.

If each of the above spectral broadening mechanisms are independent of one another, the total velocity spectrum width σ_v can be considered as a sum of σ^2 contributed by each [70]. That is,

$$\sigma_v^2 = \sigma_s^2 + \sigma_r^2 + \sigma_d^2 + \sigma_t^2 \tag{3.17}$$

where σ_s^2 is due to shear, σ_r^2 to antenna rotation, σ_d^2 to different drop size fall speeds, and σ_t^2 to turbulence. The significance of the total width σ_v for weather radar design is discussed in Sections IV and V.

It should be noted that (3.17) does not show a beam broadening term defined by Nathanson [89] because we have elected to define shear in terms of measured radial velocities in the radar's spherical coordinate system. The components σ_r^2 and σ_d^2 are related to the radar and meteorological parameters [89] as

$$\sigma_d^2 = (\sigma_{do} \sin\theta)^2 \tag{3.18}$$

$$\sigma_r^2 = \left(\frac{\alpha\lambda}{10.7\,\theta_2}\right)^2 \tag{3.19}$$

where θ_2 is the two-way half-power beamwidth in radians for an assumed circularly symmetric antenna having a Gaussian distribution of power. The width σ_{do} is caused by the spread in terminal velocity of various size drops falling relative to the air contained in V_s. Lhermitte [80] has shown that for rain, σ_{do} is about 1.0 $(\mathrm{m}\cdot\mathrm{s}^{-1})$ and is nearly independent of drop size distribution and rainfall rate. The elevation angle θ is measured to beam center, and α is the angular velocity of the antenna in radians per second. In terms of the usually specified one-way half-power beamwidth θ_1

$$\theta_2 = \sqrt{2}\,\theta_1. \tag{3.20}$$

The wind shear width term σ_s is composed of three contributions, i.e.,

$$\sigma_s^2 = \sigma_{s\theta}^2 + \sigma_{s\phi}^2 + \sigma_{sr}^2 \tag{3.21}$$

where each term is due to radial velocity shear along the elevation, azimuth and radial directions, respectively. Assumptions behind (3.21) are that shear is constant within the resolution volume and that the weighting function is product separable along θ, ϕ, and r directions. Let k_θ, k_ϕ be shears in the θ, ϕ directions and use (3.9) to obtain

$$\sigma_{s\theta}^2 + \sigma_{s\phi}^2 = (r\sigma_\theta k_\theta)^2 + (r\sigma_\phi k_\phi)^2 \tag{3.22}$$

where σ_θ^2 and σ_ϕ^2 are defined as second moments of the two-way antenna pattern in the indicated directions. A circularly symmetric Gaussian pattern has

$$\sigma_\theta^2 = \sigma_\phi^2 = \theta_1^2/16 \ln 2. \tag{3.23}$$

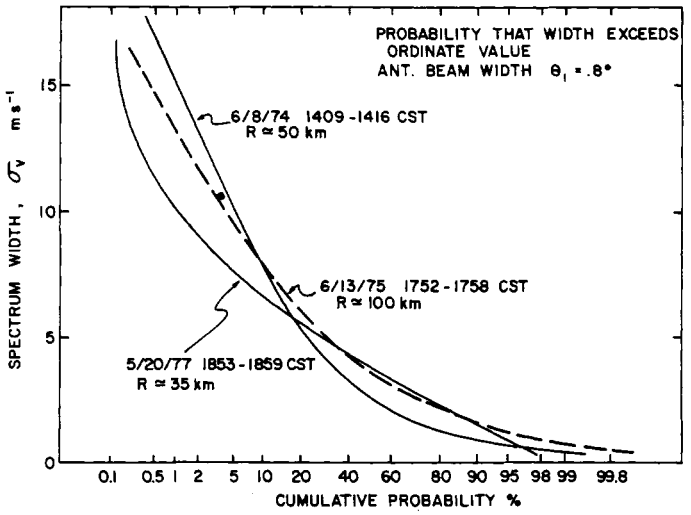

Fig. 6. Cumulative probability of unbiased spectrum widths for echoes from three tornadic storms. Spectrum widths are derived from spectra computed using discrete Fourier transforms of echo samples having $S/N \geq 15$ dB. Width estimates from the pulse pair algorithm. Equation (4.4) produce almost identical results.

Following arguments that led to (3.22), one can show that constant radial gradient of shear k_r contributes

$$\sigma_{sr}^2 = \sigma_r^2 k_r^2 \tag{3.24}$$

to the width, where σ_r^2 is the second central moment of the intensity weighting function in range. For a rectangular transmitted pulse, Gaussian input filter and under "matched" conditions (i.e., $B_6\tau = 1$) the last equation reduces to

$$\sigma_{sr}^2 = (0.34\, k_r c\tau/2)^2. \tag{3.25}$$

The width σ_t due to turbulence is somewhat more difficult to model. When turbulence is homogeneous and isotropic within the resolution volume, widths can be theoretically related to eddy dissipation rates [52].

Doviak *et al.* [48] have made measurements of total spectrum widths σ_v in severe tornadic storms and Fig. 6 data show a median width value of about 4 m · s^{-1} and about 20 percent of widths larger than 6 m · s^{-1}. They have deduced that these large widths are most likely due to turbulence that is not homogeneous and isotropic suggesting the presence of energetic eddies of scale size small compared to their radar's resolution volume. For these experiments $\theta_1 = 0.8°$ and $\tau = 1$ μs; so weather radars, not having better resolution, should obtain similar width distributions in severe storms.

Strauch and Frisch [116] have measured widths up to 5 m · s^{-1} in a convective store (3-cm wavelength radar, beamwidth 0.9°, range up to 55 km). It is significant that those maximums were in the transition region between up and downdrafts and close to the reflectivity core.

It is extremely important to relate widths to severe turbulence so that radars can give reliable measure of turbulence hazardous to aircraft. Analysis by J. T. Lee at the National Severe Storms Laboratory (NSSL) [78] suggests a strong connection between spectral width and aircraft penetration measurements of turbulence. His data show that when aircraft derived gust velocities exceeded 6 m · s^{-1}, corresponding to moderate or severe turbulence, the spectral width exceeded 5 m · s^{-1} in every case for aircraft within 1 km of the radar resolution volume. Not all storm regions of large spectral width produce aircraft turbulence. Furthermore, when σ_v was less than 4 m · s^{-1}, the aircraft experienced only light turbulence in over 50 thunderstorm penetration flights. Accurate estimates of turbulence and shear, as well as rain and hail hazards, should allow safer flights through showers produced by thunderstorms.

For most situations, the combination of radar characteristics and meteorological parameters result in negligible contribution from all mechanisms except k_θ and k_ϕ shear of the radial velocity, and turbulence [107]. Because the two angular shears can be determined directly from the angular dependence of the mean radial velocity, the component due to turbulence can be extracted from spectral width. A value of k_θ shear equal to 1×10^{-3} s^{-1} is suggested by Nathanson [89], yet NSSL's Doppler velocity fields show k_θ shears of about 1 to 2×10^{-2} s^{-1} which typify mesocyclone regions of tornadic storms.

IV. Doppler Moment Estimation

The pulsed Doppler radar should supply (for each radar resolution volume) three spectral moment estimates of prime importance: 1) the echo power or zero moment of the Doppler spectrum (this is an indicator of water content in the resolution volume), 2) the mean Doppler velocity or the first moment of the spectrum normalized to the zeroth moment, and 3) spectrum width σ_v, the square root of the second moment about the first of the normalized spectrum, a measure of velocity dispersion within the resolution volume.

The Doppler spectrum's zero and second moment can be estimated also with incoherent radars employing envelope detectors [104]. By far the most used spectral moment is the zeroth or echo power estimate $\hat{P}(\tau_s)$. The $\hat{P}(\tau_s)$ values of meteorological interest may easily span a range of 10^9 and often the choice of receiver hinges upon the cost to meet this large dynamic range requirement. Logarithmic receivers are quite effective in accommodating such a large dynamic range, thus the Doppler radar may sometimes have a separate logarithmic channel for reflectivity estimation, whereas a linear channel is well suited for velocity measurements. Moment estimates utilize samples of a randomly varying signal and the confidence or accuracy with which these estimates represent the true moments directly depends on the SNR, on the distribution of velocities within the resolution volume, on the receiver transfer characteristics, and on the number of samples processed M. In the case of weather echoes, single sample estimates have too large a statistical uncertainty to give meaningful data interpretation. Thus a large number of echo samples must be processed to provide the required accuracy.

To obtain a quantitative estimate of $\bar{P}(\tau_s)$, samples must be averaged over a period long compared to the echo decorrelation time which is the reciprocal of spectrum width. The probability density and moments of the averaged output and of the input power estimate can be derived from the known weather echo statistics and the receiver transfer function [85]. The output signal Q of radar receivers can have one of many functional dependencies upon the signal applied to the receiver's input. The problem is to estimate $\bar{P}(\tau_s)$ from sample averages of Q. The estimation is complicated because Q is not linearly related to $P(\tau_s)$ (except for square law receiver). That is, when mean output estimates $\hat{Q}$ are used with the receiver transfer function (i.e., Q versus $P(\tau_s)$) to obtain estimates $\hat{P}(\tau_s)$, we generate biases and have larger uncertainty in the estimates $\hat{P}(\tau_s)$ than if we averaged $P(\tau_s)$ directly [107],

[127]. Because considerable correlation may exist from sample to sample, the variance reduction achieved by averaging is less than it would be for independent samples [80]. The degree of correlation between samples is a function of radar parameters (i.e., wavelength, PRT, beamwidth, pulsewidth, etc.) and the meteorological status (e.g., degree of turbulence, shear, etc.) in the resolution volume.

Estimate variance can be reduced, at the expense of resolution, by averaging along range time as well as sample time. Because the resolution volume's range extent is usually small compared to its angular width, averaging over a range interval Δr usually results in a more symmetrical sample volume with little degradation of the spatial resolution. Range-time averaging the output of a linear or logarithmic receiver introduces a systematic bias of the estimate caused by reflectivity gradients, which will limit the maximum Δr useful for averaging [100]. Nevertheless, we have a reasonable latitude available in choosing Δr.

Only Doppler radar can provide first spectral moment estimates, but at the expense of considerable signal processing. The algorithmic structure of a maximum likelihood (ML) mean frequency estimator is in general unknown, but important special cases have been documented in the literature. For instance, when a pure sinusoid is immersed in white noise, the ML algorithm calls for a bank of narrow-band filters; the center frequency of a filter with maximum output is then the desired estimate [66]. Discrete Fourier transform processing generates, conveniently, a bank of parallel filters but is not used in the ML sense to extract the mean frequency because weather signals have considerable bandwidth. Rather, a straightforward power weighted mean frequency provides the estimate. Miller and Rochwarger [87] and Hofstetter [71] have established the autocovariance argument as a ML estimator for certain conditions. This estimator is popularly known as the PP algorithm. It is ML when pulse pairs are independent, i.e., when the covariance matrix of time samples is tridiagonal with the same off diagonal elements. Also, as shown by Brovko [20], the optimality of PP extends to a first-order Markov sequence in case the white noise is negligible.

Second moment estimators are of necessity more complex and, therefore, their optimum properties are more difficult to establish. Estimates based on Fourier methods and PP processing have proven to be useful, and it is known that for independent PP's, the PP width estimator is ML [71], [87]. These two methods of spectral moment estimation are discussed in detail in the remainder of this section.

A. Mean Velocity Estimation–Doppler First Moment

1) Fast Fourier Transform: The FFT algorithm is used to evaluate the discrete Fourier transfrom (3.16) [34]. Mean velocity calculation by the spectral density first moment usually involves some method of noise and ground clutter removal. More common methods are *thresholding* by power or frequency [109] or noise suppression by subtraction of expected noise power from the spectral density coefficient [14]. Performance of two FFT mean velocity estimators is shown in Fig. 7 for Gaussian signal spectra and white noise.

2) Covariance or Pulse-Pair Estimator: The complex covariance and the spectral density constitute a Fourier transform pair and thus by the moment theorem, the moments of the spectral density correspond to the derivatives of the complex covariance evaluated at zero lag.

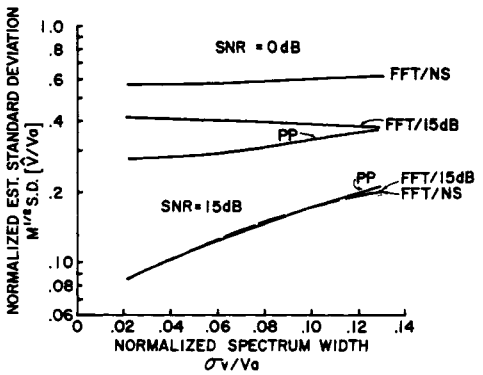

Fig. 7. Standard deviation of FFT and covariance PP mean velocity estimators at two SNR's. Normalization parameter is the Nyquist velocity v_a and square root of number of samples $M^{1/2}$. NS signifies estimate after noise power subtraction; 15 dB is after application of a 15-dB threshold below spectral peak. Gaussian signal spectrum and white noise are assumed.

An ML unbiased estimator[2] of $R(T_s)$ [87]

$$\hat{R}(T_s) = \frac{1}{M} \sum_{n=1}^{M} V[(n+1)T_s]\, V^*[nT_s] \tag{4.1}$$

forms the basis of the algorithm for an estimate of mean velocity $\bar{v}$ given by

$$\hat{v}_{PP} = \frac{v_a}{\pi} \arg [\hat{R}(T_s)] \tag{4.2}$$

where $2v_a = \lambda/2T_s$ is the unambiguous velocity span (Nyquist interval). The covariance argument is an unbiased estimate of the first moment for symmetrical spectra [14], a condition usually satisfied by meteorological signals.

General statistics of covariance estimates for statistically independent sample pairs with a Gaussian signal covariance function and white noise are given by Miller and Rochwarger [87]. Equally spaced samples, forming contiguous pairs in which each sample is common to two pairs, of a time signal having a Gaussian spectral density and white noise are treated by Berger and Groginsky [14] and both correlated and uncorrelated pairs are treated by Zrnić [130]. Statistical properties of the covariance argument estimator are also shown in Fig. 7. Satisfactory estimation of mean velocity can be made with input spectrum widths up to about 0.4 of the Nyquist velocity. However, uncertainty of the estimate increases rapidly for larger widths, requiring long dwell times for quantitative estimates. This can be seen from the exponential growth of variance at large widths [130].

$$\mathrm{VAR}\,[\hat{v}_{PP}] = \frac{\lambda^2 \exp\,[(4\pi\sigma_v T_s/\lambda)^2]}{32\pi^2 M T_s^2} \cdot \left\{ \left(\frac{N}{S}\right)^2 + 2\,\frac{N}{S}\,(1 - \exp\,[-8(2\pi\sigma_v T_s/\lambda)^2]) + \frac{4\pi^{3/2}\sigma_v T_s}{\lambda} \right\}. \tag{4.3}$$

In addition to performing well with populations having wide widths, the PP estimator is superior (in terms of estimate standard deviation) to the FFT at low SNR (Fig. 7). One of

[2] This is strictly true if successive pairs give independent estimates of $R(T_s)$. It has not been shown that similar properties ensue for correlated sample pairs.

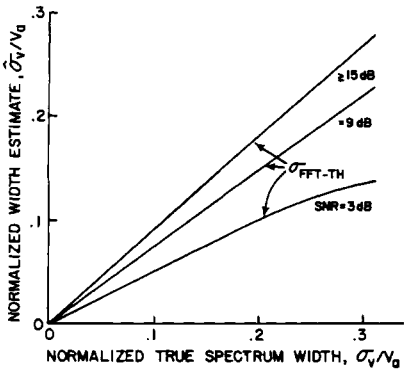

Fig. 8. Expectation of spectrum width by FFT-TH (normalized to Nyquist velocity) versus true width for simulated Gaussian spectra and white noise; a sliding threshold equal to SNR was applied below the spectral peak.

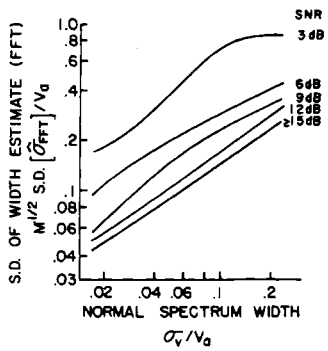

Fig. 9. Standard deviation of width estimate by FFT-TH versus true spectrum width.

the major advantages of this estimator, though, is the ability to operate on pairs of samples as opposed to the equally spaced pulse train required for straightforward FFT analysis.

It is worth mentioning that the PP algorithm is a special case of Burg's maximum entropy method; i.e., when the weather signal is modeled as a first-order autoregressive process, the equation that locates the spectrum peak from the forward and backward prediction coefficients is the same as (4.2), [23].

B. Spectrum Width Estimation—Second Moment About the Mean

1) FFT Width: A spectrum width estimate is the square root of the second moment about the mean velocity. In practice this computation usually involves some type of noise suppression. Thresholding the spectrum by power tends to bias systematically the width estimate low since part of the signal spectrum as well as noise is removed [110]. The expected width estimate by FFT is given in Fig. 8 as a function of true width with Gaussian spectra and a threshold at the SNR below the spectrum mode. The standard deviation of the FFT width estimate is shown in Fig. 9.

2) Covariance Techniques for Estimating Width: Like the mean frequency, the second spectral moment can be estimated directly without recourse to Fourier transform. For Gaussian spectra and when PP's in autocovariance calculations are independent, one can show using the results of Miller and Rochwarger that the following spectrum width estimate is ML [87]

$$\hat{\sigma}_v = \frac{\sqrt{2}\,v_a}{\pi}\sqrt{|\ln(\hat{S}/|\hat{R}(T_s)|)|}\ \operatorname{sgn}\{\ln[\hat{S}/|\hat{R}(T_s)|]\}. \quad (4.4)$$

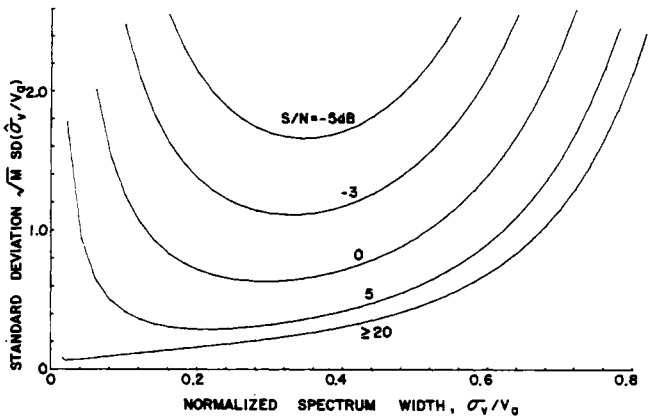

Fig. 10. Standard deviation of width estimate by PP from contiguous PP's. At large and narrow widths the SD increases rapidly. Range of normalized input widths where estimates are precise is from about 0.06 to 0.6. Because this is a perturbation solution, it takes a large number of pairs M for the results towards the spectrum to be valid; acually at zero width the standard deviation is proportional to $M^{-1/4}$ rather than $M^{-1/2}$ [130].

$\hat{S}$ is the signal power estimate obtained from the complex video signal after subtraction of the known noise power N. Statistics of this estimator for independent PP's was examined by Rummler [103]. A related estimator

$$\hat{w} = \frac{\sqrt{2}\,v_a}{\pi}\left|1 - \frac{|\hat{R}(T_s)|}{\hat{S}}\right|^{1/2} \operatorname{sgn}[1 - |\hat{R}(T_s)|/\hat{S}] \quad (4.5)$$

does not depend on spectrum shape provided that the width is sufficiently smaller than the Nyquist interval. Velocity spectra associated with weather echoes have a wide range of spectrum widths, but since it has been our experience that shapes are mostly Gaussian, version (4.4) is recommended because it eliminates the asymptotic (i.e., $M \to \infty$) bias caused by the finite difference approximation for the derivatives. Perturbation analysis on Gaussian spectra shows both (4.4) and (4.5) have identical variances and very similar number of sample (M) dependent bias. For the most part, the bias is not serious because it is proportional to M^{-1}, as is the variance. Fig. 10 illustrates the standard deviation of width (4.4) when the autocovariance is calculated from contiguous pairs. Note again that coherency limits the useful range of input spectrum width to about 0.6 of the Nyquist velocity, while noise increases errors at narrow widths [130]. Very similar results are obtained if noncontiguous or independent pairs are considered.

C. Errors in Estimated Moments

Besides inherent uncertainties due to the stochastic character of weather signal, the moments are subject to biases generated at various stages of processing and errors due to extraneous spurious signals. Jitter in the oscillator chain broadens the spectrum and so does the clipping prior to or in the analog-to-digital converters. This and other nonlinearities generate harmonics. DC offsets and line frequency pickup bias the mean and width but can usually be controlled by proper design and ground clutter filters [110]. Imbalances in the phase and amplitudes of the video signals create undesirable image spectra. If the amplitudes are balanced to within 10 percent and the phase to better than 5 percent, the image peak is more than 25 dB below the signal [129].

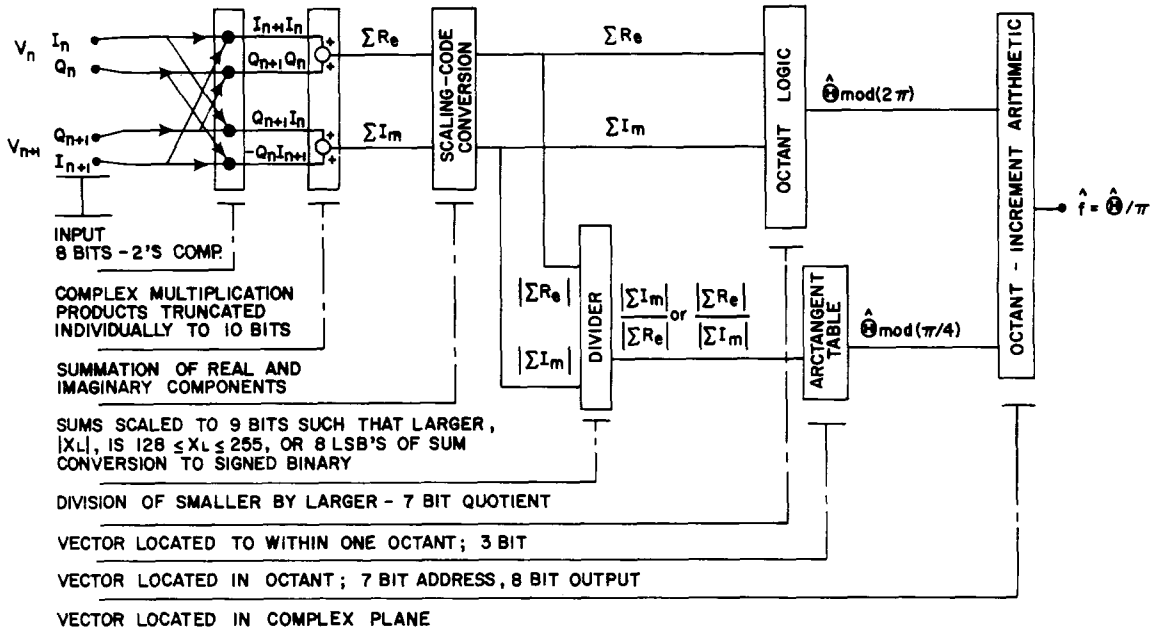

Fig. 11. A flow diagram for hardware implementation of the covariance mean frequency estimator.

D. Hardware Implementation of Covariance Mean Estimators

One aspect common to any hardwired implementation is the digital quantization. Reduction of the length of input or output words or any intermediate numerical result has the advantage of decreasing the amount of hardware and thus both cost and complexity.

One method of implementing the covariance mean estimator in hardware is just straightforward expansion of the algorithm (4.1) into a series of real operations (Fig. 11). To select digital processing parameters it is convenient to describe the quantization effects statistically from which bias and variance due to quantization can be easily modeled. The bias, for fixed point arithmetic with a b bit word and the usual assumption of uniform density across the digital class, is zero for round off and $\frac{1}{2}$ digital class width 2^{-b}, for truncation. The quantization variance is $2^{-2b}/12$. Word length is established on the basis of quantization variance relative to the inherent signal variance at each point in the computation. See the following example.

Consider the flow diagram of Fig. 11. Two of the digital parameters which should be selected primarily from required performance (meteorological) criteria are input word length, on the basis of expected signal dynamic range, and output word length such that this quantization standard deviation (SD) is small compared to the required SD of the Doppler estimate. The output word specifies the arc tangent table output increments and thus the table input increments. Internal n word lengths are then specified by these two variance boundaries.

For the scheme and word lengths on Fig. 11, the truncation that dominates quantization variance occurs in the digital multiplier. The product is truncated to make the quantization SD compatible with estimate SD. Care must be taken in selecting this product length to preserve the dynamic range of the input because a significant estimate bias (comparable to output estimate SD) at low level signals appears when the product is truncated to the input word length. An example for the Fig. 11 scheme is on Fig. 12. This bias increases sharply as the product length is truncated to the input word length. A measure of the variance introduced by product truncation is reflected in the ratio of the SD of mean frequency estimate

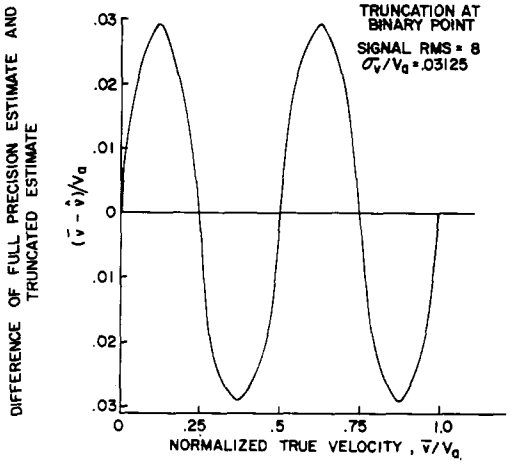

Fig. 12. Bias of mean velocity estimate with truncation of complex product terms to input word length. Results apply to both full precision calculations after the multiplier and hardwired calculator.

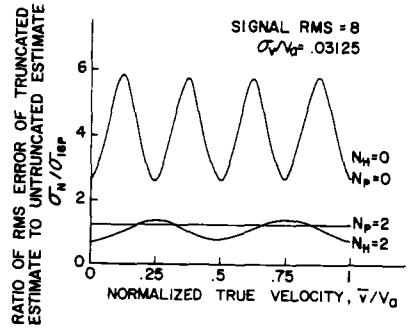

Fig. 13. Ratio of standard error of mean velocity estimate with truncated product terms σ_N to standard deviation of estimate with product of 16 bits and full precision, σ_{16P}. N_H is the difference (number of bits) between input work length and product terms in hardware scheme. Np is the difference with full precision.

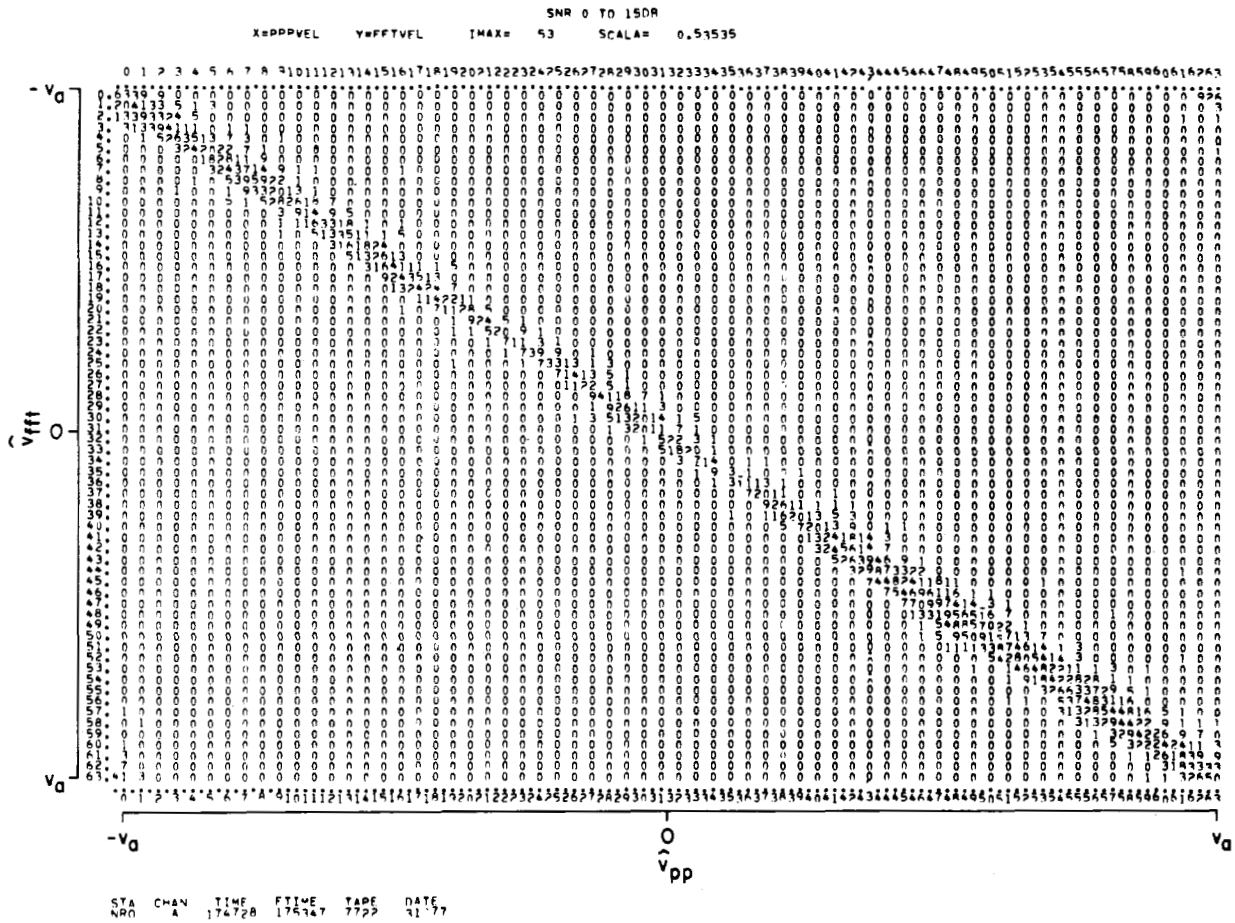

Fig. 14. Scattergram of hardware pulse pair velocity and power spectrum derived velocity for the same resolution volumes in a storm. *S/N* power ratios are between zero and 15 dB.

with truncated hardwire logic to the estimate SD using full computer precision (Fig. 13). The sharp increase in estimate SD for product truncation from 10 bits to 8 bits coupled with the bias increase at this point indicates that a product word length of input word plus two bits is a good compromise between data load and quantization variance for this scheme.

An example of the performance of NSSL's hardwired PP processor is shown in Fig. 14. This is a scattergram of mean velocities in thunderstorms estimated by the hardwired processor versus the mean velocity at the same radar pulse volumes as derived by FFT analysis. The SNR for this data set is between 0 dB and 15 dB, and the computer labels along the axes are the offset binary numbers used in the numerical data handling. Velocity is given on the auxiliary axis where 34 $m \cdot s^{-1}$ is the Nyquist velocity of NSSL's Doppler radar.

V. Considerations for Observations of Severe Thunderstorms

This section examines limitations, due to range-velocity ambiguities, in pulsed Doppler radar observations of severe storms and presents techniques to mitigate these restrictions. Radar waveform designs [39], formulated to remove ambiguities when targets are discrete and finite in number or when cross sections do not span a large dynamic range, do not work well with weather targets which are distributed quasi-continuously over large spatial regions (tens to hundreds of kilometers), and whose echo strengths can span an 80-dB power range.

A. Ambiguities

To illustrate the point, Fig. 15 is a conglomerate of thunderstorm cells as seen by a WSR-57 radar. One of the cells produced a tornado that was tracked with a nearby Doppler radar (see Section VI-B2b). The Doppler radar's unambiguous range extends only to 115 km (Fig. 16) as opposed to the 900 km on the WSR-57. Although the Doppler radar range is ambiguous beyond 115 km, the tornado producing cell at 150 km in this particular case is not completely overlaid (obscured) with echoes from other trips ($cT_s/2$ intervals). Furthermore, because the radar is fully coherent from pulse to pulse, velocity measurement is possible within unobscured regions of this second-trip storm. Target range becomes ambiguous when true range exceeds $r_a = cT_s/2$, but these ambiguities can be resolved if different trip echoes are not overlaid so as to be scrambled.

Target velocities are ambiguous because we cannot distinguish between real Doppler shifts and those aliases spaced in frequency by the pulse repetition frequency. Thus the range velocity product

$$r_a v_a = c\lambda/8 \tag{5.1}$$

typifies the ambiguity resolution capabilities of conventional (i.e., uniform pulse spacing) Doppler radars. The equation shows the advantage of longer wavelengths, but other factors may control this choice.

Fig. 15. WSR-57 PPI display of thunderstorm cells on a tornadic day (181704 CST April 19, 1976). Gray shadings (dim, bright, black, dim, etc.) represent dBZ levels differing by about 10 dBZ starting at 17 dBZ. Range marks are 100 km apart, elevation angle = 0.0°. Unambiguous range is 910 km. The boxed area outlines a tornadic storm cell whose mesocyclone signature was detected in real time by NSSL's Norman (NOR) Doppler radar which is nearly colocated with the WSR-57.

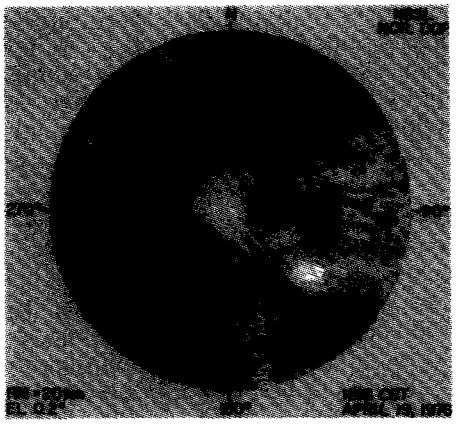

Fig. 16. Same storm system (181635 CST) seen with the Doppler radar having 115-km unambiguous range. 10-log Z brightness categories (dim, bright . . .) start at 10 dBZ and increment at about 10-dBZ steps. The 10-log Z scale applies only to first-trip echoes. Some range-overlaid echoes can be recognized by their radially elongated shape. The box outlines the same area as in Fig. 15. Range marks are 20 km apart. Part of the tornadic storm is obscured by a nearby (30–60-km range) storm.

B. Echo Coherency Considerations

In principle one can choose T_s large enough so no second or higher order trip echoes would ever be received, but this choice is limited in that signal samples spaced T_s apart must be correlated for precise Doppler shift measurement. Correlation exists when [5]

$$\frac{\lambda}{2T_s} \gg \sigma_v \tag{5.2}$$

where σ_v is the velocity spectrum width of echoes at range r. Condition (5.2) merely states that Doppler width should be much smaller than the Nyquist interval $\lambda/2T_s$. Correlation decreases appreciably when $2\sigma_v T_s/\lambda \geqslant (2\pi)^{-1}$ and the variance in mean Doppler velocity estimates $\hat{v}$ increases exponentially as can be seen from (4.3). A similar formula (with the exception of the exponential term because sampling was ignored) was derived by Denenberg [40] for variance in mean velocity estimates computed from Doppler spectra. This leads one to consider the inequality

$$\frac{\lambda}{2T_s} \geqslant 2\pi\sigma_v \tag{5.3a}$$

or, in terms of the unambiguous range

$$\frac{c\lambda}{4r_a} \geqslant 2\pi\sigma_v \tag{5.3b}$$

as a condition to maintain signal sample correlation. Width estimate variance also has an exponential increase when corrections are made to account for bias [130]. Requirement (5.3) means that σ_v limits the largest unambiguous range for a given wavelength, whereas (5.1) restricts r_a only if ambiguities due to velocity aliases need to be suppressed by choosing a large v_a. As shown below, there are methods to resolve velocity aliases (provided σ_v is sufficiently small (see Section V-D4)). Thus (5.3), a necessary condition to maintain signal sample correlation or echo coherency, must dictate r_a for a chosen λ or vice versa, not (5.1). Spectrum width σ_v is dictated by the weather. Unless spectrum widths are less than a few meters per second, it is unlikely that 10 cm or smaller wavelength radars will eliminate (i.e., by having an $r_a \geqslant 500$ km) overlaid storm echoes.

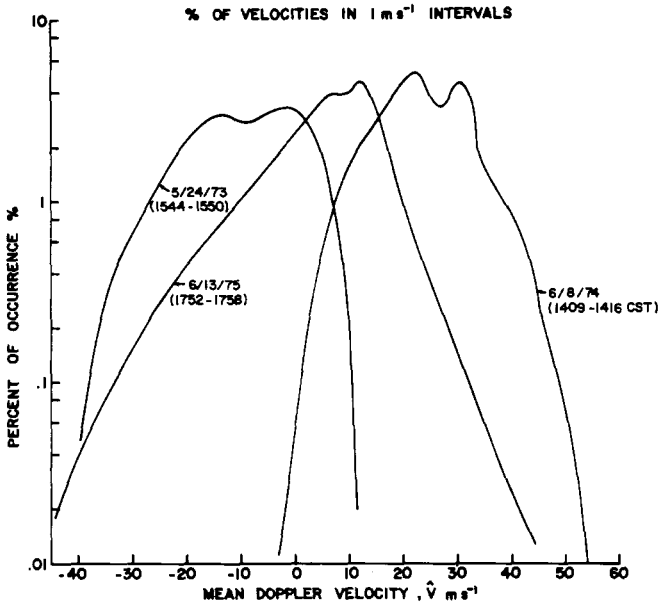

Fig. 17. Relative frequency of occurrences (percentage) of mean Doppler velocity for three tornadic storms. Data samples are uniformly spaced through most of the convective cell. Note the large spread of radial velocities which needs to be measured unambiguously.

C. Distribution of Velocity in Severe Storms

Histograms of mean velocity shown in Fig. (17) illustrate what is to be expected from severe storms when viewed by a narrow beam (0.8°) antenna [48]. Some 20 000 sample points from resolution volumes near ground to about 10 km are used, and the estimates are from PP's. The center of the velocity distributions (Fig. 17) are displaced relative to one another and to zero due, in part, to storm motion. More important than the mean motion, or peak radial speeds, is

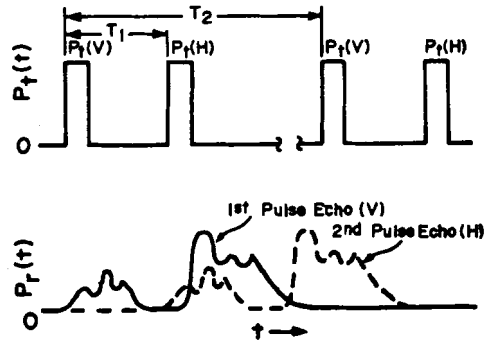

Fig. 18. Signal diagram for orthogonally polarized (V, H) samples of a pulse pair; P_t is transmitted power and P_r, received mean power. Weather-type targets are assumed to produce the echo pattern of P_r.

the larger than 50 m · s^{-1} spread in velocities for any of these storms. Conventional Doppler radars may require an unambiguous velocity span of at least ±35 m · s^{-1} in order to limit velocity aliasing to a few percent or less.

D. Extension of Maximum Unambiguous Range and Velocity

In the absence of practical methods to simultaneously eliminate range-velocity ambiguities, several schemes have been devised to alleviate the aliasing problem. A list of those more promising follows.

1) Random Signal Radar: This radar uses random modulation of a CW signal [29] and requires continuous calculations of the autocorrelation for each range of interest. This extensive signal processing, the lack of any "clear area" [39], and the need for two antennas has limited the use of this radar in meteorological research.

2) Phase Diversity: If an r_a, v_a combination can be found which will provide the desired range coverage with acceptable velocity aliasing, the phase of multitrip signals with equally spaced transmitted pulses can be decorrelated by retention in the local oscillator, transmitter phase information for only one system period while transmitter phase is randomly shifted from pulse to pulse. Alternately the transmitter phase history may be shifted by one or two system periods in another receiver and measurements thus made in the second or third-trip regions. Echoes outside the selected trip are then incoherent and when overlaid one over the other only produce an effective SNR decrease that does not bias mean velocity estimates. This technique is especially suited for good magnetron transmitters and has been used on several systems [83], [27].

3) Spaced Pairs: The use of spaced PP's of orthogonally polarized samples (Fig. 18) for weather radars can reduce occurrence of overlaid echoes [44]. This technique has been successfully adapted to radars measuring ionospheric motions [123]. Also, the Wave Propagation Laboratory has implemented it (without orthogonal polarization diversity) in their 3-cm Doppler radar [27].

The first advantage of the method is that, with T_2 sufficiently large, overlay is limited to targets in contiguous range invervals ($cT_1/2$) or trips. That is, first- and second-trip targets can have overlaid echoes as well as second- and third-trip targets, etc., but there is no echo overlay for targets in first- and third-trip intervals or second and fourth, etc. Second, all overlaid echoes are incoherent if T_2 is sufficiently large (i.e., $T_2 \gg \lambda/4\sigma_v$). Thus they do not bias velocity estimates and only serve to decrease the effective SNR. When the pulses of a pair are orthogonally polarized, (polarization diversity), overlaid echo power can be decreased, possibly by as much as 20 dB [44]. This may make insignificant the occurrence of pesky overlaid echoes.

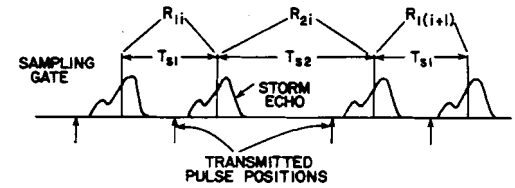

Fig. 19. A possible spacing of sampling gates for a staggered PRF system to obtain covariance $\hat{R}_1$, $\hat{R}_2$ estimates at two different lags.

A disadvantage of spaced pairs is that a longer time will be required to collect sufficient number M of sample pairs so that velocity estimate variance is reduced to acceptable limits. However, one does not need the same M as in the case of uniformly spaced pairs because sample pairs are less correlated [130]. Furthermore, by changing the carrier frequency between pairs of pulses, we can space pairs closer, thus significantly increasing the number of sample pairs without worsening obscuration. Another disadvantage of this technique is that ground clutter canceler design is more complicated.

4) Staggered PRT: A velocity estimate $\hat{v}_1$ is obtained from PP estimates of complex covariance $\hat{R}_1$ at lag T_{s1} while $\hat{v}_2$ is derived from covariance $\hat{R}_2$ for pairs spaces T_{s2}. To decrease estimate variance, covariance estimate $\hat{R}_1$ (or $\hat{R}_2$) is an average of M sample pair covariance estimates (R_{1i} (or R_{2i})) (Fig. 19). Because $\hat{v}_1$, $\hat{v}_2$ are associated with different Nyquist cointervals, velocity aliases may give significantly different estimates—differences that can be attributed to the different aliases [48]. Mean velocity aliases can be resolved so long as the expected difference $E[\hat{v}_2 - \hat{v}_1]$ remains unambiguous. However, errors in resolving aliases may occur because one cannot estimate $E[\hat{v}_2 - \hat{v}_1]$ with zero variance [111].

To illustrate what can be gained with staggered PRT, consider the two unambiguous Nyquist velocities v_{a1} = 16 m · s^{-1} and v_{a2} = 24 m · s^{-1}. The maximum unambiguous Nyquist (composite) velocity v_a becomes ±48 m · s^{-1}. Now a single PRF radar with a Nyquist velocity v_m = ±35 m · s^{-1} has an unambiguous range of 100 km if wavelength is 10 cm and 50 km if it is 5 cm. On the other hand, the staggered PRT radar would have the unambiguous range increased by a factor of $v_m/v_{a2} \approx 1.5$ or an increase in area by 2. This improvement is obtained at the expense of dwell time.

In summary, a staggered PRT technique can significantly increase the unambiguous range, and the maximum unambiguous velocity v_m can easily be made large so that velocity aliasing is of little importance.

As of now, there is no conclusive study to determine whether spaced pairs (with or without polarization diversity) would give Doppler radars sufficient immunity from velocity-range ambiguities in severe storms and whether this approach is more (or less) advantageous than staggered PRT, phase diversity, or random signal radar. Because the intrapair spacing T_1 in the space pair technique is forced to be small to achieve the same unambiguous velocity as obtained with staggered PRT, we undoubtedly expect a larger occurrence of scrambled echoes for the spaced pair method.

5) Dual-Sampling Technique: Even though obscuration of Doppler signatures by overlaid multiple trip echoes might not be eliminated, there is reason to present the observer a velocity data field wherein range to datum is unambiguous and velocity values are credible (i.e., are not in error due to scrambled

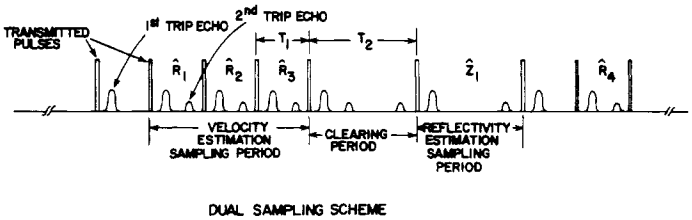

Fig. 20. Dual sampling technique, where $\hat{R}_1, \hat{R}_2, \hat{R}_3, \ldots$, are covariance measurements (at equal lags) whose average is used to derive mean Doppler velocity estimates. We depict only first and second-trip echoes and assume $T_2 = 2T_1$. Clearing period T_2 removes multiple-trip echoes from reflectivity estimation in a contiguous T_2 interval.

echoes). This can be accomplished by taking echo reflectivity samples during an interval T_2 sufficiently long to remove, for practical purposes, all overlaid echoes and have this sampling period interlaced with another whose PRT is short enough to allow coherent measurements for velocity estimates (Fig. 20). By interlacing the velocity estimation period MT_1 with one for reflectivity (T_2), we can have nearly colocated resolution volumes for velocity and reflectivity measurements. The figure shows one block of samples that contain $M = 3$ covariance estimates and one reflectivity estimate (for each range bin). To reduce velocity and reflectivity estimate variance, we need to average covariance and reflectivity estimates for K blocks. In order to have all n-trip echoes samples ($n = 2$ in Fig. 20) in one T_1 period, sampling should start in the nT_1 interval because the nth multiple-trip echo will not appear until then. Dual sampling provides echo reflectivity measure without range ambiguities so we can determine, through comparison of echo powers, those velocity data that are significantly contaminated by scrambled multiple-trip echoes and eliminate them from observation. Furthermore, we can assign correct ranges to the surviving valid velocity data. Such a dual-sampling system is in operation at NSSL ($N = 7$, $K = 8$, $T_1 = 768\ \mu s$, $T_2 = 4T_1$) and velocity fields displayed in real time are not range ambiguous. The most persistent obscuration to plague the dual sampling radar is caused by ground clutter echoes overlaid onto the second trip (i.e., ground clutter seen just beyond r_a) as well as ground clutter within the first trip. Ground clutter obscuration can be lessened with cancelers and by displacing (through changes in T_1) the second-trip ground clutter ring away from the storm of interest; otherwise, we have a permanent ring of about 10–15 km in range wherein the Doppler radar is blinded.

A closely related method of increasing the range to which reflectivity can be resolved unambiguously is to transmit coherent signals at two different frequencies ω_2, ω_1 each at different PRT's so that simultaneous reception is possible. The long PRT yields large unambiguous range for reflectivity estimates while the high PRT is used for velocity estimation. This technique and its signal processing are analogous to the dual-sampling technique described above: its advantage is a reduction of the acquisition time and possibility for better canceler design.

The dual-sampling mode can accommodate a staggered PRF during the velocity estimation period to allow increase both in r_a and v_a at the expense of increased data acquisition time (i.e., less scans–about 30 percent less–per observation period) for given velocity estimate accuracy. These might be important gains for a dual-sampling radar, but an issue is whether obscuration is significantly decreased. Studies with simplified storm models suggest that the decrease in obscuration of first-trip echoes is small if $r_a > 130$ km, but there could be a significant improvement in decreasing obscuration of second-trip storms. In any case, an advantage of incorporating a staggered PRT is the automatic de-aliasing of velocity estimates.

VI. Observation of Weather

The great utility of storm observation with centimeter wavelength pulsed Doppler radar derives from its capacity to map reflectivity (η) and mean radial velocity $\bar{v}$ inside the storm's shield of clouds. A three-dimensional picture of a single storm takes about 2 to 5 min of data collection time not only because of antenna rotation limitations, but also because a large number of echoes from each resolution volume needs to be processed in order to reduce the statistical uncertainty in the η and $\bar{v}$ estimates. Although storm structure can change significantly during this period with distortion of the radar image of the true reflectivity and velocity fields, highly significant achievements have been made in depicting the structure and evolution of the thunderstorm.

But the meterologically interesting variables are not η nor $\bar{v}$, but parameters such as rainfall rate (on the ground) and wind. Pulsed Doppler radar most often measures the radial speed of hydrometeors, not air, and in certain situations such as vertically directed beams, these speeds can differ significantly from the radial component of wind. Likewise, surface rainfall rate estimates are not easily related to η, and often radar reflectivity measurements are supplemented by surface rain gages [18], [37].

Incoherent radars map η but, if the radar's resolution volume is sufficiently small and reflectivity estimates are accurate, these radars can track prominent reflectivity structures to map winds that steer cells [35]. However, Doppler radar measures, practically instantaneously, velocities in each resolution volume and hence can provide better resolution of the velocity field.

A. Dual Doppler Radar

A single Doppler radar maps a field of velocities that are directed toward (or away from) the radar. A second Doppler radar, spaced far from the first, produces a field of different radial velocities because the true velocities are projected on different radials. The two radial velocity fields can be vectorially synthesized to retrieve the two-dimensional velocities in the plane containing the radials [2]. It is customary to accomplish the synthesis on common grid points to which radar data are interpolated. Radial velocities in each of the radar's resolution volumes surrounding a grid point are not measured simultaneously but are separated in time up to the few minutes required for each radar to scan the common volume. The respective resolution volumes are also usually quite different in size and orientation.

Nevertheless, useful estimates of wind can be made on scales of air motion large compared to the biggest resolution volume dimensions if the velocity field is nearly preserved over the period required for data collection. Targets such as water drops having small mass quickly respond to horizontal wind forces and faithfully trace the wind. Stackpole [114] has shown that, for energy spectrum of wind scales following a $-5/3$ law to at least 500 m, more than 90 percent of the rms wind fluctuations are acquired by the drops if their diameters are less than 3 mm. When radar beams are at low elevation angles, target terminal velocities (i.e., the steady-state vertical velocity relative to the air) give negligible error in the radial

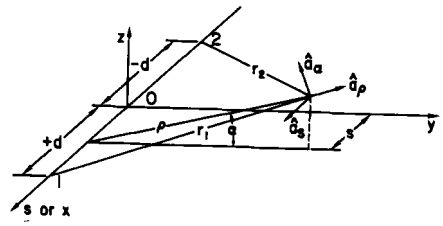

Fig. 21. Cylindrical coordinate system used for dual radar data analysis. The radars are located at points 1 and 2, and $\hat{a}_\rho$, $\hat{a}_s$, $\hat{a}_\alpha$ are the unit normals defining direction of the three orthogonal velocity components.

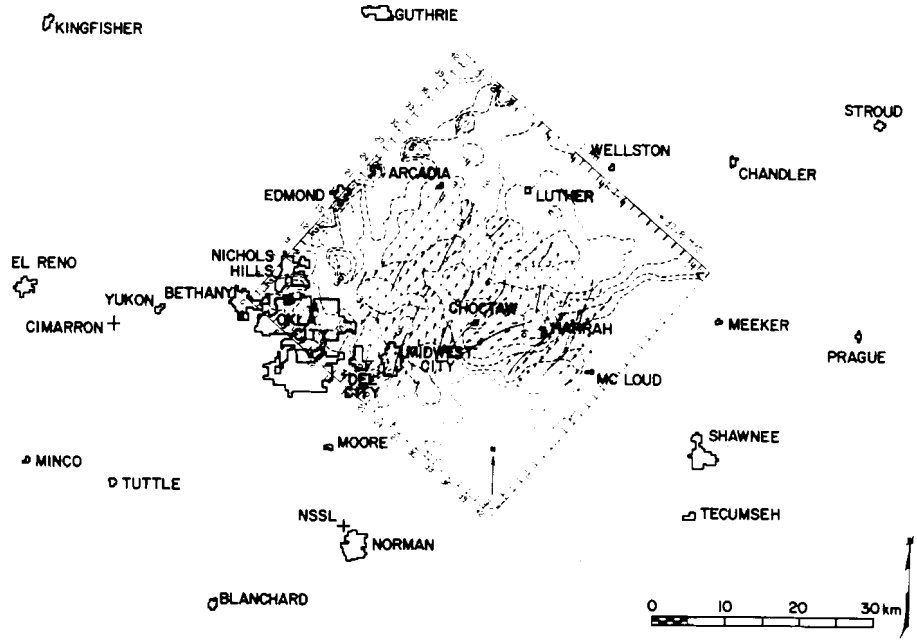

Fig. 22. Map of central Oklahoma with reflectivity field (shaded areas) and winds relative to the ground at a height of 1 km. Velocity scale vector is shown along eastern corner of box. This velocity is the maximum at this height. Reflectivity contours (dashed lines) are labeled as log Z (from Ray *et al.* [97]).

wind component. At high elevation angles these velocities need to be considered.

1) Reconstruction of Wind Fields: The dual Doppler radar technique to derive quasi-horizontal winds was first illustrated by Lhermitte [82] and later extended by Frisch *et al.* [53] to display all three Cartesian wind components. Wind field determination is greatly simplified if the synthesis is performed in cylindrical coordinates with an axis being the line connecting the two radars. That is, radial velocities at data points (centers of resolution volumes) are interpolated to nearby grid points on planes having a common axis (the COPLAN technique) [82]. Cartesian wind components can be derived from these synthesized cylindrical components. Although one could solve directly for Cartesian wind components, this necessitates a solution of an inhomogeneous, hyperbolic partial differential equation to derive vertical wind [2].

The cylindrical coordinate system is illustrated in Fig. 21. The mean Doppler velocity needs to be corrected for the scatterers terminal velocity relative to the air in which they are located. The corrected radial velocity estimate is

$$v_{1,2} = v'_{1,2} + v_t \sin\theta \tag{6.1}$$

where $v'_{1,2}$ are the mean Doppler target velocities measured by radars 1, 2 at data points. To estimate v_t for each resolution volume, one could use the empirical expression [7]

$$v_t = 2.65 Z^{0.114} \left(\frac{\gamma_0}{\gamma}\right) [\mathrm{m \cdot s^{-1}}] \tag{6.2}$$

where the parenthetical term is a correction suggested by Foote and duToit [51] to account for height dependent air density γ, and Z is the reflectivity factor. This relation well represents experimental data over a large range of Z (i.e., $1 \leqslant Z \leqslant 10^5$ mm^6 m^{-3}) for regions of liquid water, but large errors, up to several meters per second, in v_t estimates can be caused by erroneously relating regions of hail with a v_t, Z relation appropriate for liquid water. Usually there is little or no information to identify these regions uniquely, and errors in vertical wind w_z can result. However, it has been shown for typical arrangements of storms relative to the two radar placement, that the error in w_z is significantly smaller than errors in v_t [46].

The estimated radial velocities $v_{1,2}$ of the air can be interpolated to uniformly spaced grid points in planes at angle α to the horizontal surface containing the baseline. Interpola-

tion filters the data and reduces variance [46]. The cylindrical wind components in the ρ, s plane are related to $\bar{v}_1, \bar{v}_2$, as

$$w_\rho = \frac{(s+d)r_1\bar{v}_1 + (s-d)r_2\bar{v}_2}{2d\rho} \tag{6.3}$$

$$w_s = \frac{r_2\bar{v}_2 - r_1\bar{v}_1}{2d} \tag{6.4}$$

where $\bar{v}_{1,2}$ are the interpolated Doppler velocities of air.

The wind component w_α, normal to the plane, is obtained by solving the continuity equation in cylindrical coordinates:

$$\frac{1}{\rho}\frac{\partial}{\partial\rho}(\rho\gamma w_\rho) + \frac{1}{\rho}\frac{\partial}{\partial\alpha}(\gamma w_\alpha) + \frac{\partial}{\partial s}(\gamma w_s) = 0 \tag{6.5}$$

with an appropriate boundary condition [97]. The mass density γ is given by

$$\gamma = \gamma_0 \exp[-gM\rho \sin\alpha/(RT)] \tag{6.6}$$

and g is the gravitational constant (9.8 m · s^{-2}), M the mean molecular weight of air (29 $gmol^{-1}$), T the absolute temperature (K), and R the universal gas constant (8.314 J · mol^{-1} · K^{-1}). Appropriate values of γ_0, T can be obtained from surface site and upper air soundings. The Cartesian components of wind can then easily be obtained from w_ρ, w_s, w_α.

2) Observation of a Tornadic Storm: The first dual Doppler radar observations of a tornadic storm were made on April 20, 1974, with NSSL's 10-cm radars. These radars provide a large unambiguous range and velocity capability well suited for observation of the large and severe thunderstorms that frequent the high plains of the United States.

Fig. 22 locates the two radars, one at Cimarron airfield (CIM), Oklahoma City and the second (NRO) at NSSL's headquarters, Norman, OK. It also shows the horizontal wind field synthesized using a slight modification of the above outlined scheme [97].[3] Streamlines have been drawn in addition to velocity vectors, whose length is proportional to wind speed. The curvature in the streamlines shows appreciable local vorticity in the region near the grid point (30.0, 24.0).

To view the storm's kinematic structure at several altitudes the mean wind at each height is subtracted from the wind vector at each grid point. This perturbation velocity field is displayed at two heights in Fig. 23(a). Cyclonic circulation is apparent at the grid point (30, 24), where vorticity was noticed in Fig. 22. Inflow into the tornadic cyclone is shown at an altitude of 3 km, and divergence and outflow are apparent at 7-km height. High reflectivity factor (60-dBZ) regions are located on the downwind side. These velocity fields are in general agreement with present storm models, particularly in the weak echo region where both imply a strong updraft northeast of the circulation (Fig. 23(b), $X = 33$, $Y = 27.0$ km). A downdraft (Fig. 23(b), $X = 33$, $Y = 22.5$ km) is found to the southwest of the circulation.

3) Errors in Synthesized Wind Fields: The wind fields derived from dual Doppler radar measurement have errors that arise from several sources. Some of these are: 1) variance in the mean Doppler velocity and Z estimates due to the statistical nature of the weather echo, 2) nonuniform reflectivity factor Z within a resolution volume, 3) use of incorrect v_t, Z relationship, 4) inaccuracies in resolution volume location, 5) increase of vertical velocity variance with height owing to error in derivative estimates in the continuity equation, 6) nonstationarity of the storm during a data collection scan, and 7) echoes received through sidelobes that contaminate signals associated with the resolution volume. How these errors affect the estimates of horizontal and vertical wind is discussed in [46].

[3] Terminal velocity corrections were obtained from interpolated reflectivity factor values and a slightly different v_t, Z relationship was used.

B. Observations with a Single Doppler Radar

Although the Doppler radar measures only the radial wind component, its spatial distribution can signify important meteorological events such as tornado cyclones. Moreover, high straight winds, if not across the beam, can be measured as well as turbulent regions. Thus a single Doppler radar offers good promise for severe weather warning and in our view will most likely become the operational tool of the National Weather Service in the near future.

1) Linear Wind Measurements–Velocity Azimuth Display: When the antenna beam is scanned in azimuth ϕ while elevation angle θ is fixed, the radial velocity has the ϕ dependence

$$v_r = w \sin\theta + v_h \cos\theta \cos(\phi - \delta - \pi) \tag{6.7}$$

where δ is the wind direction, w the vertical velocity, and v_h the horizontal speed of tracers in the resolution volume. The w and v_h velocities are readily computed from data in a velocity azimuth display (VAD) [84] under the assumption that air is in pure translation. (The VAD is a display of radial velocity at a single range location versus azimuth.) Then (6.7) has a sinusoidal dependence on ϕ; thus amplitude and phase of the sine curve are measures of v_h and δ at the height $r \sin\theta$ of the sampling circle. Vertical motion produces a dc offset of the sine wave. However, when wind is not horizontally homogeneous, equation (6.7) is no longer purely sinusoidal.

Caton [28] showed how divergence can be determined from VAD data. Browning and Wexler [22] carried the analyses even further by assuming the wind field was well represented by a linear velocity field [68, p. 198] over the circle of measurement. Under this assumption there are four basic fields of motion that convey air: pure translation, vortical, divergent, and deformative. Fourier analysis of (6.7) for linear wind reveals that of these four motions only the vortical one cannot be measured by the VAD method. The average component of (6.7) is proportional to mean horizontal divergence $\overline{\mathrm{DIV}\, v_h}$ plus mean $\bar{w}$, that is

$$\frac{1}{2\pi}\int_0^{2\pi} v_r\, d\phi = \frac{r}{2}\cos\theta\,(\overline{\mathrm{DIV}\, v_h}) + \bar{w}\sin\theta \tag{6.8}$$

where $\bar{w}$ is the average of vertical velocity on the sampling circle of radius r. The first harmonic component gives v_h and δ, and the second measures deformation. By inserting the mass continuity equation into (6.8), we can then solve for vertical wind if we have an estimate of target terminal velocity averaged over the circle. If the target is refractive index fluctuations (see Section VI-C), then clearly terminal velocity is zero. Thus a single Doppler radar can measure the three components of wind averaged over a sampling circle of radius r and produce a vertical profile of wind.

2) Severe Storm Cyclone Observations and Presentations: Because the radar maps the distribution of Doppler velocity

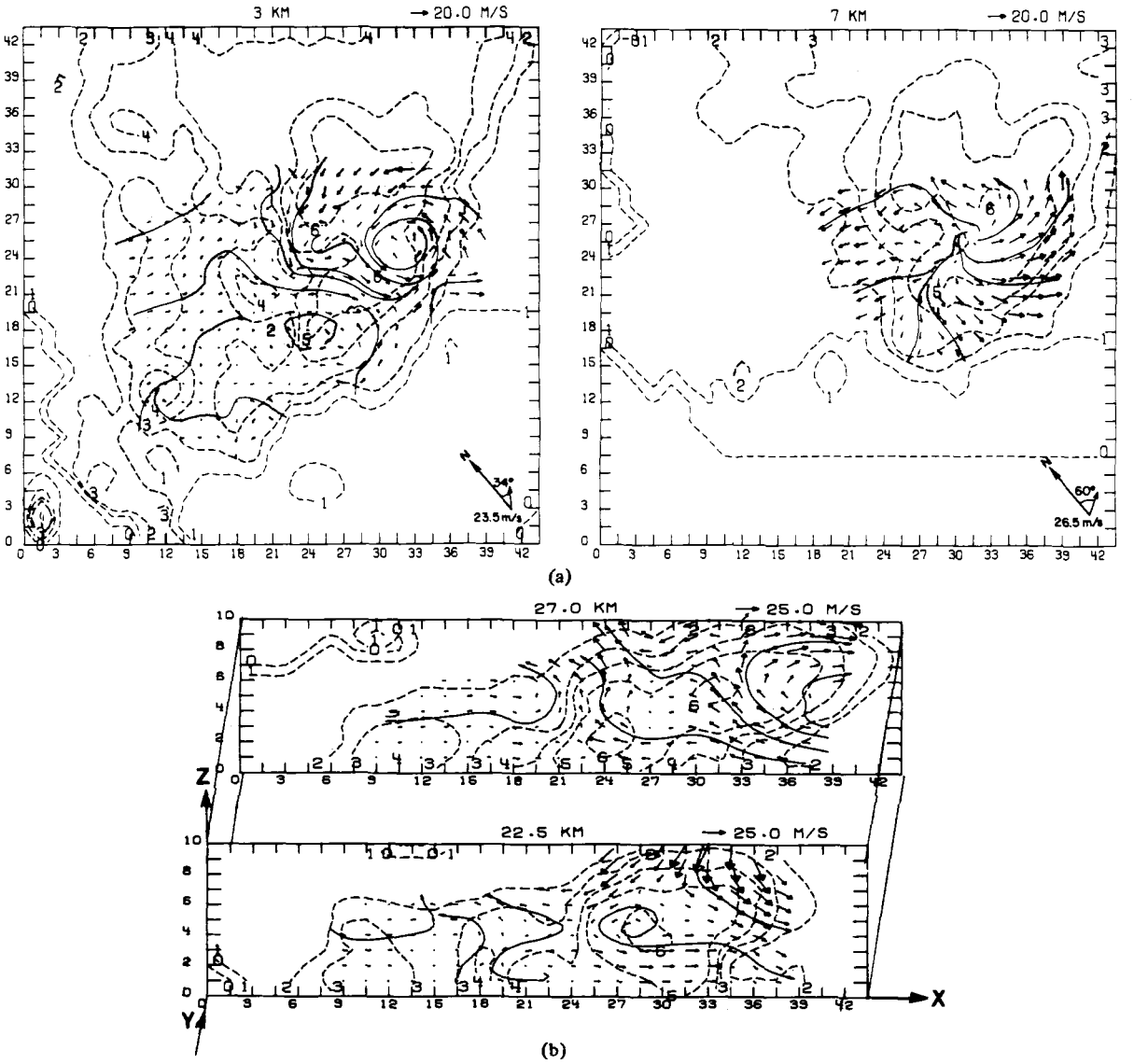

Fig. 23. (a) Perturbation wind and reflectivity factor (log Z) at 2 different altitudes. Mean wind at each altitude is shown in lower right corner. Velocity scale is in upper right corner. Distances are in km from an origin $s = -10$, $\rho = 15$ km ($s = 0$ is the midpoint of the base line) and abscissa is parallel to s. (b) reflectivity and velocity fields in the x, z plane for two planes. The mean horizontal velocity in each vertical plane was removed and is indicated in the upper left of each plane. Reflectivity contours are labeled as log Z (from Ray *et al.* [97]).

inside the storm, significant meteorological events (unseen from outside) such as tornado cyclones should produce telltale signatures. Donaldson [42] stipulated criteria whereby a vortex can be identified from single radar observations. Briefly, there must be a localized region of persistently high $\geqslant 5 \times 10^{-3}\ s^{-1}$ azimuthal shear (i.e., the velocity gradient along an arc at constant range) that has a vertical extent equal to or larger than its diameter.

It can be shown that nontranslating cyclones have isodops forming a symmetric couplet of closed contours with equal number of isodops encircling positive and negative velocity maxima (Fig. 24). If the inner portion of the vortex is a solidly rotating core, its tangential velocity linearly increases with radius to a maximum. Outside this maximum, the velocity decreases (roughly) inversely with the radius. The isodop contours of such a combined Rankine vortex are circular sections connected with straight lines (Fig. 24). This pattern has been observed many times, and an example is shown in Fig. 25(a) for a tornadic storm that did considerable damage to Stillwater, OK, in 1975 [21], [24], [133]. Fig. 25(b) shows contours of Doppler σ_v for the same storm, and we immediately see the striking correlation of large σ_v with significant radial velocity shear. Regions of large σ_v may also indicate the presence of strong turbulence.

a) PPI weather display: Reflectivity factor is now routinely displayed by the National Weather Service radars on the PPI scope and by some television stations on a color PPI display. While reflectivity cannot be reliably used for tornado detection, it has proved valuable for hydrological studies and severe weather warnings. Those warnings are primarily based on reflectivity values, storm top heights, and sometimes on circulatory features or *hook* echoes.

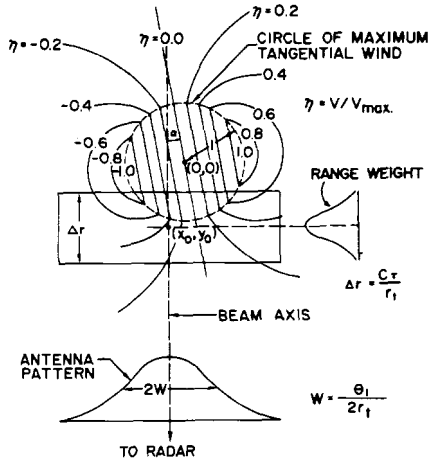

Fig. 24. Plan view of idealized isodop pattern for a stationary modified Rankine vortex located at range large compared to vortex diameter. η is Doppler velocity normalized to peak tangential wind. Radar is located towards the bottom of the figure. Resolution volume, antenna and range weighting functions are depicted. The angular tilt α determines radial inflow ($\alpha < 0$) or outflow ($\alpha > 0$).

Because PPI scopes are commonly used with radars, it is no surprise that weather researchers have begun displaying velocity fields on them. One of the early displays was obtained when a mean velocity processor of the National Severe Storms Laboratory was mated to the PPI [108]. In this case brightness level signifies a particular radial velocity category (e.g., Fig. 26(b)). If the wind and reflectivity were uniform over a full 360° of the scanned space, the display would show intervals of radial velocity as angular sectors of different brightness for each velocity category. Strobed brightness as a function of azimuth is used to differentiate positive from negative velocities (unstrobed brightness).

NSSL's real-time Doppler velocity processor was operational during the Spring of 1973, generating the first velocity contour maps of mesocyclone signatures. The Marlow tornadic storm on June 4 produced a particularly large mesocyclone, and its reflectivity and isodop signatures are clearly shown in Fig. 26. This storm's reflectivity structure exhibits a hook echo feature suggesting mesocyclonic circulation, severe weather, and tornadoes. Although the hook echo is identified usually as an appendage to the storm, it may, as in this case, be found within the storm. Average storm height during data collection was 16 km; motions of signature and storm were equal (280°/13 m · s^{-1}), with both considerably to the right of mean environmental wind (250°/12.5 m · s^{-1}). East of the high reflectivity core, a low reflectivity notch extends well into the storm. Storm motion relative to the radar is slight, and therefore, isodop patterns indicate radial velocity relative to the storm. The nearly symmetric isodop signature indicates circularly symmetric cyclonic rotation consistent with that inferred from the reflectivity pattern.

A signature pattern for circularly symmetric convergence is similar to the vortex pattern but rotated clockwise by 90° [45]. The reflectivity spiral suggests convergence, a view supported by the clockwise angular displacement of isodop maxima about the vortex center (190°, 82 km). Color displays of reflectivity, velocity and spectrum width allows, in real time, an easier quantitative evaluation and better resolution of cyclones.

b) The multimoment Doppler display: Large changes in the first Doppler moment from resolution volume to resolution volume, and large second moment magnitudes have been judged potentially important as tornado signatures. Sufficiently intense azimuthal shear is the feature used to locate the tornado vortex signature (TVS); this has been correlated with many tornadoes [21]. Large spectrum width is another distinguishing feature of a tornado predicted by Atlas [4] and

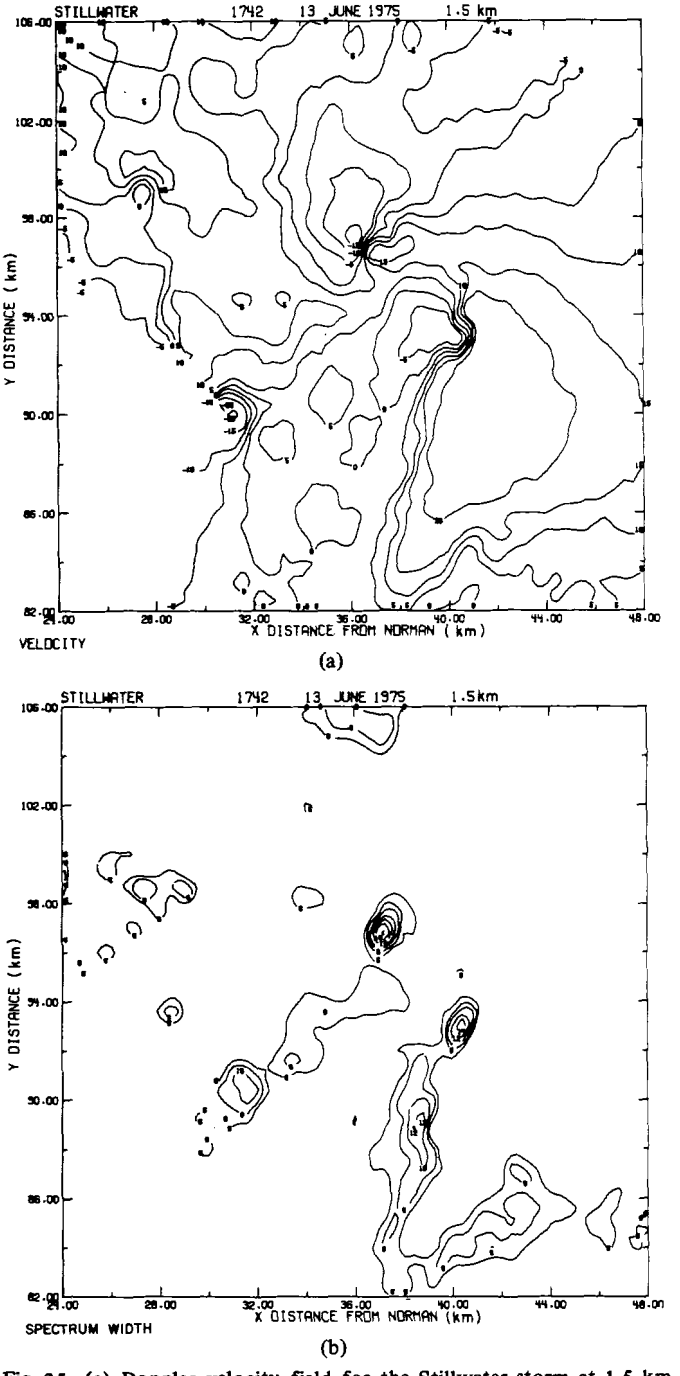

Fig. 25. (a) Doppler velocity field for the Stillwater storm at 1.5 km height. Grid spacing is 400 m. Velocities are in m·s^{-1} and contours (isodops) are in 5 m·s^{-1} steps. The mesocyclone is centered at $Y = 97$ km, $X = 36$ km. The other shear region from 94 km north, 40 km east to the bottom of the field was identified from dual Doppler data to be the low-level boundary (gust front) between storm inflow to the east of the shear line and outflow to the west. (b) Contours of constant spectrum width at 1.5 km above ground. Values equal to or larger than 6 m·s^{-1} in steps of 2 m·s^{-1} are displayed for visual clarity. Large widths farther north are where the tornado mesocyclone formed; the other region of large width is embedded in the gust front. Interpolation grids are spaced at 400 m.

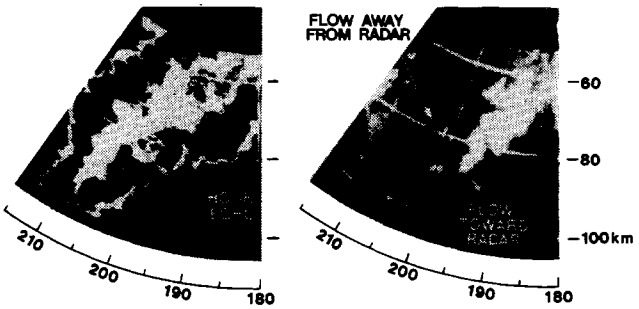

Fig. 26. Storm reflectivity (a) and isodops (b) displayed on PPI at 2115 CST. The elevation angle is 1.9°, range marks correspond to 60, 80, 100 km. Reflectivity factor categories are: dim (<21 dBZ), bright (21-31), black (31-44), dim (44-57), and bright (>57 dBZ). Velocity categories are dim <13 ms^{-1}), bright (13-21), and brightest (>21). Positive radial velocities are angularly strobed in brightness. Mesocyclone signature is between 194°-203° and 73-90 km.

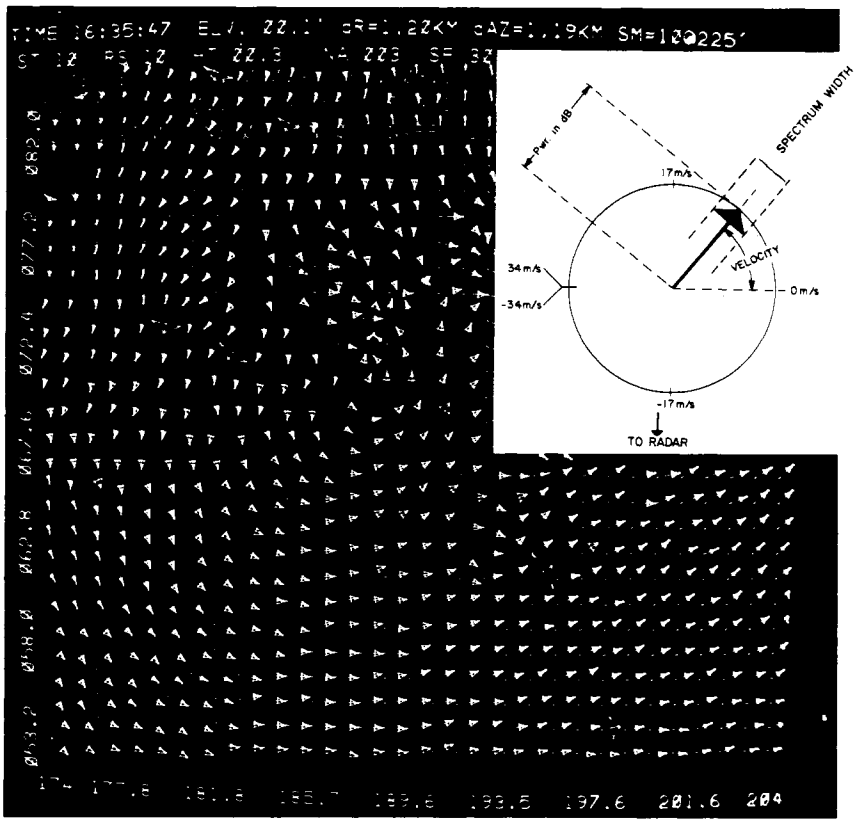

Fig. 27. The multimoment Doppler display of a mesocyclone. Each arrow contains information of the 3 principal Doppler spectrum moments for a resolution volume. For interpretation of arrows see insert in upper right corner (arrow length is proportional to received power, arrow direction to velocity and arrowhead size to Doppler spectrum width). Abscissa is azimuth and ordinate scale denotes range (km) from radar. Housekeeping information is at top of screen.

Lhermitte [81] (see Fig. 5). The various signatures of mesocyclones and tornadoes may be revealed at once by using three separate displays or, as described below, with a single display called a multimoment Doppler display (Fig. 27).

To present simultaneously the three principal Doppler moments for each resolution volume, a field of arrows is displayed where arrow length is proportional to the logarithm of echo power, arrow direction to velocity, and arrowhead size to spectrum width (see insert on Fig. 27 and [26]). Zero velocity is a horizontal arrow pointing right and nonzero velocities are proportional to the angle between the arrow direction and its zero position. A horizontal arrow pointing left corresponds to the Nyquist velocity ($\pm 34\ m \cdot s^{-1}$). As the velocity increases beyond $\pm 34\ m \cdot s^{-1}$, the arrow rotates smoothly through the Nyquist limits and appears as a lower velocity of opposite sign (e.g., $38\ m \cdot s^{-1}$ appears as $-30\ m \cdot s^{-1}$). In these displays, the radar is always toward the bottom of the figure so that arrows in the upper half of the circle denote flow away from the observer, whereas arrows in the lower half denote flow towards the radar. Thus the field of arrows in Fig. 27 illustrates quite nicely the signature of circulation (centered at 187°-Az 70-km range) or con-

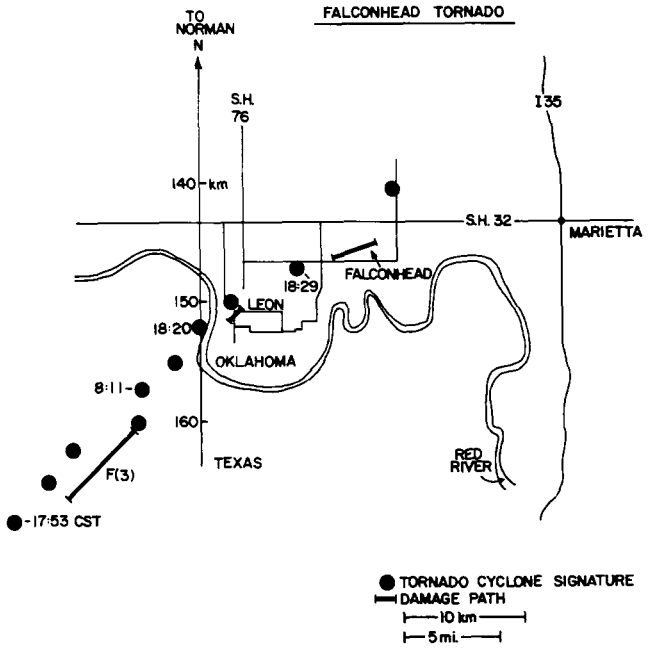

Fig. 28. Mesocyclone signature track for the Falconhead tornado showing damage path location relative to the cyclone signature center (April 19, 1976). The reflectivity field of the storms for that day is shown on Figs. 15 and 16, where the boxed areas contain the storm that produced the only tornado on this day.

vergence (188° Az and 75-km range). The radial component of storm motion (SM: 10 m · s^{-1} from 225°) has been subtracted from all velocities.

A tremendous advantage is obtained with Doppler radar because it can sort out among many storms the ones that have intense circulation and hence potential for tornado development. Fig. 15 shows a large storm system composed of many individual convective cells. The multimoment display depicts the principal moments in a sector of space that can be placed over any storm so that the principal moments can be simultaneously examined for evidence of significant meteorological phenomena. Each storm can be systematically interrogated and for the example shown in Fig. 15 only the storm outlined by the box produced a tornado. This tornado's mesocyclone signature was tracked for almost an hour, and Fig. 28 shows the position of the signature relative to the damage path. Even though the storm was in the Doppler radar's second trip, the beamwidth was sufficiently small (0.8°) for tracking at ranges to 170 km when the signature was first noticed.

Although the Doppler radar had an unambiguous range of 115 km on this day, storm distribution was such that none were range-overlaid onto this mesocyclone, thus allowing an unobscured measurement of its velocity signature. The overlaying of storms due to small unambiguous range (see Section V) associated with Doppler radars can result in obscuration of signatures.

3) Doppler Spectra of Tornadoes: In 1961 Smith and Holmes reported a tornado spectrum that was obtained with a CW Doppler radar [112]. It was twelve years later that a tornado was first observed by a pulsed Doppler radar [132].

Radar views principally that portion of circulation which lies within the resolution volume so that tracers moving with the same velocities contribute to spectrum components according to their reflectivity, isodop density, and antenna pattern illumination (see Fig. 24). Only those targets whose spectral power is above the receiver noise level may be positively identified. However, it has been our experience, that tornadoes in a resolution volume offer enough reflectivity, due to debris and hydrometeors, that a large velocity span can be observed. Presently it is not known whether tracers moving at the peak tornado wind speed can be resolved.

When centered on the beam axis, the Rankine vortex model predicts a bimodal spectrum which was verified experimentally several times [132], [133]. Shown on Fig. 29 are Rankine model vortex spectra matched to data by a least squares fit. The examples of spectra are from the Stillwater maxitornado. Deduced from the fitting are maximum velocity of 92 m · s^{-1} and tornado diameter of 300 m. The deduced maximum velocity is larger that the radar's unambiguous velocity (±34.4 m · s^{-1}); therefore, aliasing was introduced in the model spectrum and the estimates are indirect.

Two spectra closest to the tornado were simultaneously least squares fitted. Simulated model vortex spectra and real spectra show very good agreement not only for two where the fit was made but also for adjacent gate locations (Fig. 29). Resolution volumes corresponding to any of these simulated spectra are assumed to have uniform reflectivity within the volume. Differences in echo power from each resolution volume are accounted for by forcing each simulated spectrum to have power equal to its matching data spectrum. Asymmetry of spectral peaks (Az 21.1°; range 104.136 km) about zero velocity suggests that targets were centrifuged outward with a velocity of 13 m · s^{-1}.

In view of the variety of displays and signatures associated with tornadoes, it is natural to ask which technique is most promising for their detection. A project was established involving the Environmental Research Laboratories, National Weather Service, Air Weather Service, and Air Force Geophysical Laboratory to conduct experiments that should provide some answers. Operations were conducted during the Spring of 77 and 78. It became apparent that mesocyclone circulations showed very nicely on the color display of radial velocities. Multimoment display in conjunction with the color display proved most suitable for TVS recognition. Using criteria discussed in Brown *et al.* [21], the project scientists were able to detect a number of tornadoes [25]. As a matter of fact, all tornadoes that occurred within a range less than 115 km (the radar's unambiguous range) were detected. The average lead time was about 20 min. It was established that circulation starts at mid levels (6–8 km) and works its way toward the ground. At further ranges signatures of small tornadoes are lost due to poor resolution; however, large destructive tornadoes were detected up to 240 km using the 0.8° beam of NSSL's Doppler radar. Spectrum width and shear alone have not been reliable indicators of tornadoes since turbulent areas in storms exhibit large widths and could be easily mistaken for tornadoes. Based on those experiences, it is believed that an operational tornado detection system will involve interaction between human operators and an automated scheme whereby the velocity pattern of a tornado cyclone is recognized.

C. Pulsed Doppler Observation of Clear Air Wind Fields

Whenever turbulence mixes air in which there are gradients of potential temperature and water vapor density, the turbulence causes spatial fluctuations in the refractive index n. The

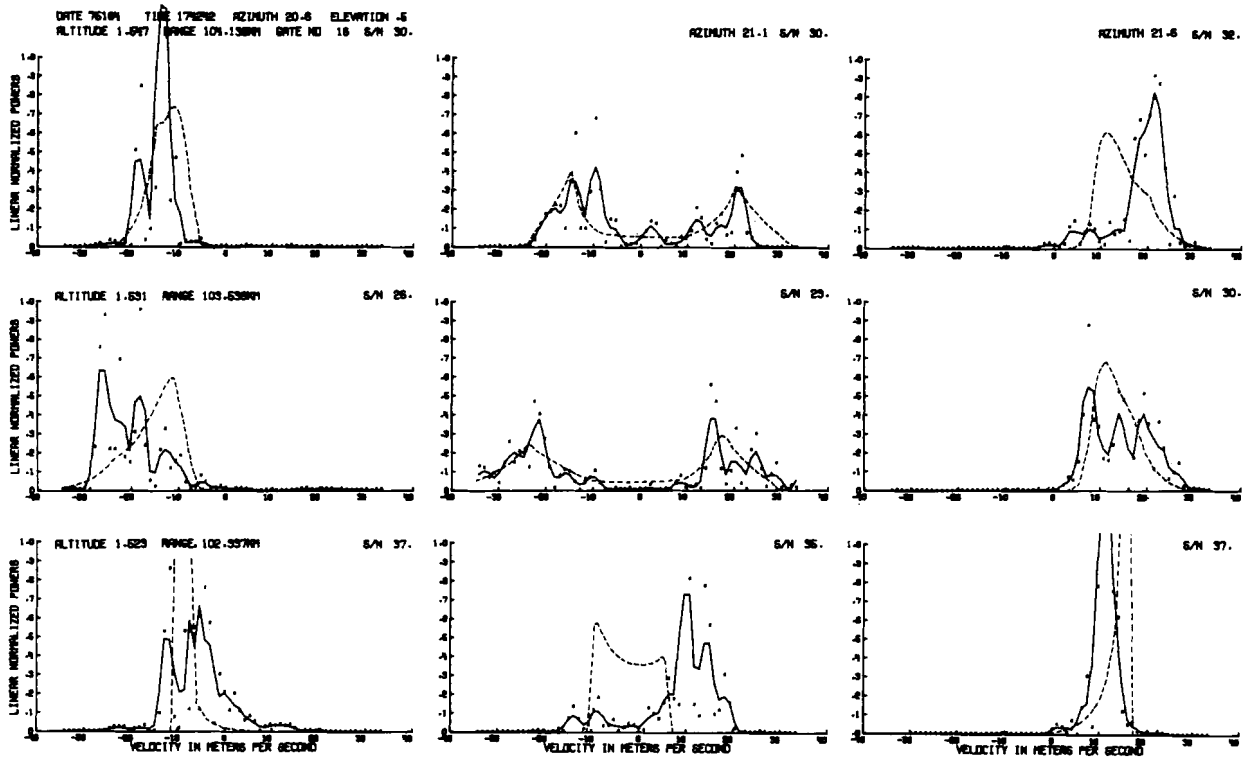

Fig. 29. Spectra from three consecutive azimuthal and range locations; Stillwater tornado. Dots show spectrum estimates from recorded time series data weighted with a von Hann window. Solid lines are three-point running averages. Dashed lines are simulated spectra. The mean square difference between data and simulated spectra is simultaneously minimized for two spectra (Az-21.1° and range of 103.5 and 104.1 km). Resolution volume depth is 150 m, range gate spacing 600 m, and antenna beamwidth 0.8°. The tornado is located between the two upper middle gates. Tornado parameters obtained from these two fitted spectra are used to compute the remaining 7 simulated spectra. Height above ground for these spectra is 640 m.

fluctuations are small (e.g., one part in a million). Nevertheless, sensitive microwave radars detect the very faint echoes returned from these irregularities in what otherwise (without turbulence) would be a smoothly changing n with negligible backscatter.

Fluctuations in temperature, humidity, and pressure need to be described in a statistical manner. Thus correlation and its Fourier transform, the power spectrum, are used to characterize the spatial variability of n. Tatarski [118] related the velocity spectrum of turbulence scales to the correlation and spectrum of refractivity scales. Furthermore, Tatarski demonstrated that, although there is a hierarchy of scales that prevail in turbulent flow, those scales equal to $\lambda/2$ contribute most to backscatter.

The parameter needed to obtain the backscatter cross section from statistically inhomogeneous media is the structure function $D_{\Delta n}$ defined as

$$D_{\Delta n} \equiv \langle [n(r + \Delta r) - n(r)]^2 \rangle \tag{6.9}$$

where $\langle\ \rangle$ denotes ensemble average. Whenever $D_{\Delta n}$ is assumed independent of r (i.e., the statistical properties of Δn are spatially uniform) we refer to the refractivity fluctuations as being *locally* homogeneous. Tatarski [118] has shown for scales within the inertial subrange of atmospheric turbulence (i.e., scales from a few millimeters to tens or sometimes a few hundred meters) that

$$D_{\Delta n} = C_n^2 (\Delta r)^{2/3} \tag{6.10}$$

where C_n^2 is the refractive index structure constant and is related to reflectivity η as [63]

$$C_n^2 = \frac{\eta}{0.38\lambda^{-1/3}}. \tag{6.11}$$

Thus if we know the structure constant of refractivity, we can, through use of (6.11) and (2.19), determine the echo power scattered by refractive index irregularities.

Echoes from clear air have been seen almost from the inception of radar observations. These *angel echoes* were first mystifying, but often were actually associated with birds and insects. Clear air echoes, not related to any visible object in the atmosphere, were conclusively proven to emanate from refractive index fluctuations through use of multiwavelength radars at Wallops Island [63]. Simultaneous measurements of refractive index fluctuations and reflectivity corroborated this finding [105]. Of course, radar studies were preceded by an enormous amount of measurement using tropospheric-scatter communication links which often depend upon clear air refractive index fluctuations to provide reliable wide-band circuits between distance points [98] (see also a special PROCEEDINGS OF THE IRE, Scatter Propagation Issue, Oct. 1955).

In the 1960's ultrasensitive incoherent radars were used to remotely detect and resolve clear air atmospheric structure and these studies are well reviewed by Hardy and Katz [64]. These radars showed meteorological phenomena such as convective thermals [73], [75], sea and land breeze [86], and Kelvin-Helmholtz waves [69].

Doppler processing of coherent radar echoes can improve target detection by at least an order of magnitude [67] and

hence medium resolution weather radars could have a detection capability matching that often associated with large aperture (18–27-m diameter) antennas used with incoherent radars. Furthermore, a coherent radar provides a way in which ground clutter can be distinguished from moving atmospheric targets and allows data acquisition at closer ranges, thereby taking advantage of the r^{-2} dependence in echo power.

Chadwick *et al.* [30] have monitored C_n^2 values in the planetary boundary layer and have concluded after one year of observation that winds can always be measured to several hundred meters height with moderately sensitive radars. Clear air wind measurement has practical significance because pulsed Doppler radars under development by the FAA also could measure wind shear hazards near airports for all weather conditions [79].

Harrold and Browning [65] found that radar can delineate the upper limit of convection, prior to precipitation, showing that it is deeper in some regions than others. Some of these areas of deep convection persist for several hours and, if showers develop, they occur within, and only within such regions. Important economic advantage can be achieved if radars can serve the dual purpose of locating weather hazards to aircraft and predicting the location of incipient showers.

Mapping boundary-layer wind over large areas has double significance for severe studies because 1) it allows early observation of thunderstorm development–hence, storm genesis can be followed from the very beginning of cumulus development; 2) the capability of Doppler weather radars to map clear air wind makes possible monitoring thunderstorm outflow and inflow which is usually precipitation free.

Strongest fluctuations in refractive index occur where turbulence mixes large gradients of mean potential temperature and specific humidity [125]. Gage *et al.* [54] measured the height distribution of forward scattered signal strength to show good correlation between it and gradients of potential temperature at high altitudes where water vapor contributions can be ignored. The tropopause is a region where potential temperature always increases with height, and it was first detected by radar in 1966 [6]. More recently Van Zant *et al.* [121], using backscatter results from a vertically pointed VHF radar, obtained consistent agreement between rawinsonde inferred C_n^2 and radar measured C_n^2 for the clear air above the moist boundary layer.

For many years ionospheric scientists have been employing high power VHF and UHF radars to observe the ionosphere. Recently these radars at Jicamarca, Peru [124]; Arecibo, Puerto Rico; Chatanika, AK [8]; and Lindau, Germany [101] have lowered their sights to examine echoes in the nonionized stratosphere and troposphere. A 6-m VHF pulsed Doppler radar specifically designed for tropospheric studies was recently assembled at Sunset, CO, and is making continuous observations of winds in the troposphere [60]. Some advantages of the VHF radar are that it can sometimes differentiate between scatter from hydrometeors and refractive index fluctuations [61], and it might be able to detect coherent scatter (second term of (2.10a)) from mean refractive index gradients at inversion layers [55].

1) Height Distribution of Refractive Index Structure Constant: In 1971 Ochs and Lawrence [93] made temperature fluctuation measurements using a sensor mounted on an aircraft and sounded the atmosphere in the lower 3 km. Their work demonstrated that the temperature contribution to refractive index structure constant was consistently above 10^{-17} $m^{-2/3}$ over land and ocean within the measured height interval. A sample profile of averaged C_n^2 due to temperature fluctuations over land in November 1971 is shown in Fig. 30. A bistatic radar was used to resolve weak scatter in the upper troposphere from strong scatter in the lower 1–2 km of the troposphere [43]. These measurements inferred a continuum of scatterers up 7 km having a C_n^2 value that could be as large as 10^{-17} $m^{-2/3}$ which compares with those values at 3 km reported by Ochs and Lawrence. Crane's [36] monostatic radar analysis for several days of observations show that C_n^2 is larger than 1×10^{-17} $m^{-2/3}$ for heights up to 15 km in the clear air. These results suggest Doppler weather radars with minimum detectable structure constant of 10^{-17} $m^{-2/3}$ might be able to monitor continuously the wind throughout the troposphere.

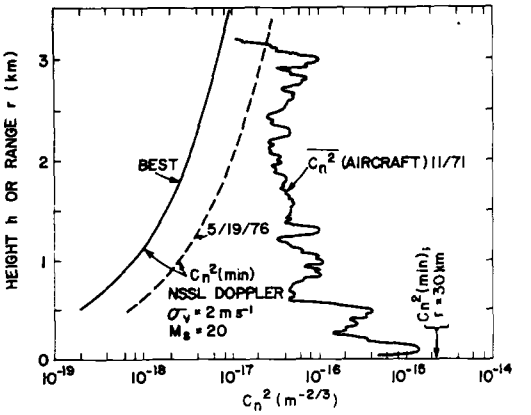

Fig. 30. Profile of average structure constant c_n^2 due to temperature fluctuations versus height h. Smooth lines are minimum radar detectable c_n^2 at range R using NSSL's Doppler system as configured on 4/19/76 (dashed line) and for system if reconfigured (solid line) to provide lower system noise temperature and higher transmitted power. (From Ochs and Lawrence [93].)

2) Frequency Modulated Continuous Wave Radar: The FM but CW radar transmits a continuous sinusoidal signal whose frequency $f = \alpha t$ is linearly swept with a period T_s. A target at range r returns a signal which is mixed with that being transmitted, to produce a difference frequency f_Δ proportional to $(2r\alpha/c)$ (see Section II-A). Thus f_Δ is a measure of target range, and ranging accuracy is determined by the dwell time T_d available to measure f_Δ. For near targets T_d is nearly equal to the time T_s required to change the microwave frequency by $\Delta f = \alpha T_s$. The decisive advantage of FM-CW radar is that range resolution can be increased simply by spanning a larger frequency Δf without decreasing average transmitted power.

Spatial resolution of the order of 1 m can be achieved easily with an FM-CW radar to show detailed structure of wave phenomena in the clear air planetary boundary layer (PBL). High resolution PBL probing with FM-CW radar was first demonstrated by Richter [99] and clear air echoes usually are found in layers, often with wave-like structure [57].

The FM-CW radar is sufficiently coherent for nearby targets. For the first time, Strauch *et al.* [115] exploited this property to measure Doppler shift of FM-CW radar echoes from the optically clear boundary layer. Linear sawtooth modulation of the microwave frequency gives the FM-CW radar characteristics that have analogy to the pulsed Doppler radar: the

Fig. 31. PPI sector scan of echo power from clear air seen by the NRO Doppler radar. Bright area of high power is aligned roughly parallel to mean wind and bands are spaced about 4 km apart. Range marks are 20 km apart. EL = 1.6° (April 27, 1977, 1447 CST).

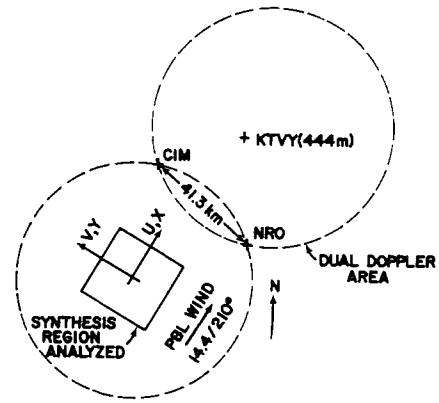

Fig. 32. The dual Doppler-radar area (dashed lines) within which the angle subtended by the radials from the Cimarron (CIM) and Norman (NRO) radars lies between 30° and 150°. The outlined box is the region wherein Doppler velocities were synthesized for detailed wind analyses. The wind speed and direction is a mean over 1.24-km depth of the PBL.

reciprocal of Δf can be considered analogous to an effective pulse length for the pulse radar, while T_s is equivalent to the PRT.

Because the FM-CW's peak-to-average power ratio is unity, we immediately infer that resolution can be increased without changing the effective per-pulse transmitted energy; not so with pulsed radar where decrease in τ reduces transmitted pulse energy. Therefore, per-pulse SNR is decreased in proportion to the square of pulsewidth, whereas the equivalent SNR of the FM-CW radar decreases linearly with effective pulse width (i.e., Δf^{-1}). This unquestionable advantage of the FM-CW vanishes when considering pulsed Doppler radar and coherent echoes. As a matter of fact, the pulsed radar may prove more advantageous [67].

3) Observations of Turbulence and Roll Vortices: Clear air winds in the planetary boundary layer (PBL, i.e., surface to heights of about 1.5 km have been synthesized from dual Doppler radar measurements [59], [76], wherein chaff was dispensed over large areas to provide suitable echo levels detection and processing). Doviak and Jobson [47] showed first results of two Doppler radar synthesized wind fields in the PBL clear air where only the diffuse and intrinsic scatterers of the medium were used as targets. They observed mean wind fields at low height to have qualitative agreement with mean wind measured (with conventional anemometers) near the surface.

On April 27, 1977, a day marked by strong nondirectional shear and curvature in the wind profile, NSSL's Doppler radar echo power measurements showed evidence of clear air convective streets (Fig. 31), an observation that should signify the presence of roll vortices. First radar detection of clear air *thermal streets* was reported by Konrad [74].

Fig. 32 locates the radars at CIM and NRO as well as a 444-m meteorologically instrumented tower. The 25 km X 25 km region (solid lined area) is where synthesized dual Doppler radar winds were analyzed in detail and is referred to as the primary synthesis region. However, reasonably accurate winds can be synthesized from Doppler data in the entire area enclosed by the dashed lines. The winds were fairly uniform from the southwest on this day, but there were small perturbations from the mean wind having a magnitude of about one order less than the mean wind itself. As is evident in Fig. 32, the x direction and u component of wind are along the mean wind and the y direction and v component normal to the mean wind.

Reflectivity is estimated from digitally averaged log-video samples at 762 contiguous resolution volumes (spaced 150 m) along the beam. Doppler velocities are measured for each of these volumes using the PP autocorrelation algorithm. Radial velocity estimates were obtained from 255 contiguous PP samples. Data are acquired at the rate of about 5 radials/s, and with the rotation rate of 2°/s, there are about 2 independent data points/beamwidth (0.8°).

Sectors stepped in elevation and scanned in azimuth by each radar encompass the primary synthesis region. Each beam scanned the same sector six times, starting at 0.5° elevation, and tilted up in 0.5° increments to 3.0°. With each radar, the tilt sequence of sector scans was begun at the same time. The synthesized wind field and its perturbations from the mean are shown in Fig. 33.

Berger and Doviak [13] have examined the spatial spectra $S(K)$, where K is the wavenumber of the synthesized winds on this convectively dry day, and have compared results with those spectra obtained from anemometers located on the tall tower. The spectra follow a 5/3 power law in the wavelength Λ range of 1 to 8 km in agreement with spectra of tower winds. Spectral analyses of clear air longitudinal wind fluctuations using chaff and a single Doppler radar have been reported by Chernikov *et al.* [32]. Their spectra, extending to 3-km wavelengths, also show a 5/3 power law dependence in agreement with results on this day. However, O'Bannon [92] shows spectra on another day when such a power dependence is not evident.

A sample set of spectra, multiplied by K and plotted on a semilogarithmic paper to show turbulence intensity per waveband, is displayed in Fig. 34. The v component spectra in the y direction have a peak at 4-km wavelength which persisted over the one hour of data collection.

Various theories (e.g., [58], [77]) suggest that roll vortices tend to form parallel to the mean wind in a strongly heated PBL having a large unidirectional shear. When vertical profiles of horizontal velocity have curvature, Keuttner [77] predicts rolls to have a horizontal spacing of 2.8 times their depth. The strong 4-km wave in the y direction of the v component might be the convective rolls predicted by theory.

Fig. 35(a) depicts perturbation winds at one of six levels synthesized from a tilt sequence of each Doppler radar. A bandpass filter was applied in the y direction to emphasize

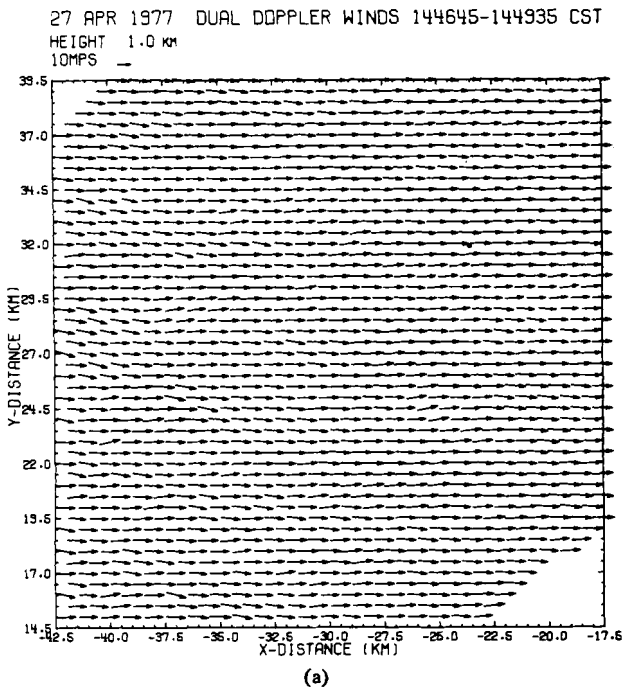

Fig. 33. (a) Dual radar synthesized wind field at 1.0 km above ground. (b) Wind with its mean removed. Synthesized wind fields were low-pass filtered once in X and Y direction with a 3-point Shuman filter [13].

the 4-km wave feature for visual display. A low-pass filter was applied in the x direction along which no dominant wavelength was noted.

Fig. 35(b) is a vertical cross section at $X = 25.5$ km perpendicular to the mean wind. Vertical velocities were derived by integrating the mass continuity equation using wind fields from the six horizontal surfaces. Vertical grid spacing is 250 m. Readily apparent are counter-rotating vortices (roll vortices) having approximately 4-km wavelength whose maximum vertical velocities are of the order of 1 $m \cdot s^{-1}$. Furthermore, the ratio of roll spacing to height is 2.6 in good agreement with that predicted by theory [77]. Gilmer *et al.* [56]

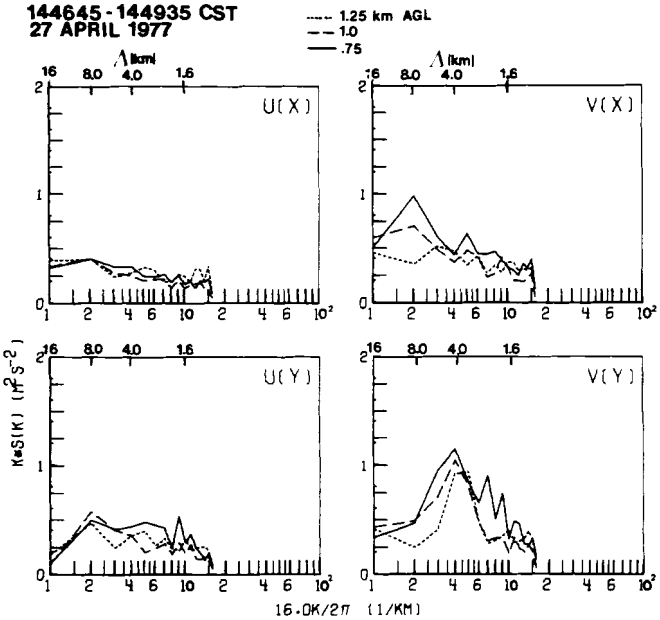

Fig. 34. A plot of KS(K) versus log K which shows distribution of power (1446:45-1449:36 CST). Note large power in velocity fluctuations at wavelength $\Lambda = 4$ km.

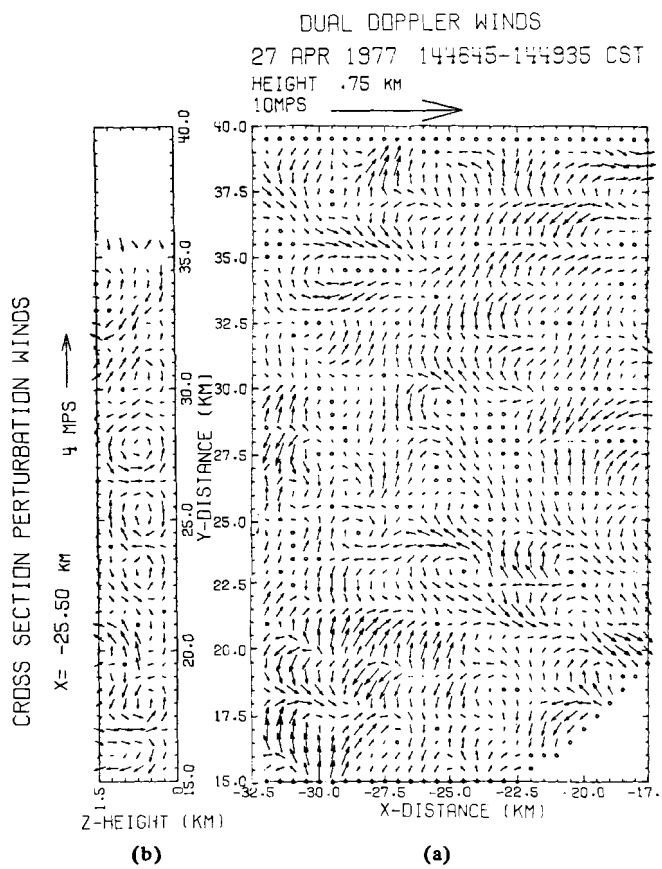

Fig. 35. Horizontal (a) and vertical (b) cross sections of bandpass filtered wind data that highlights the clear air roll structure seen in the spectra displays of unfiltered data.

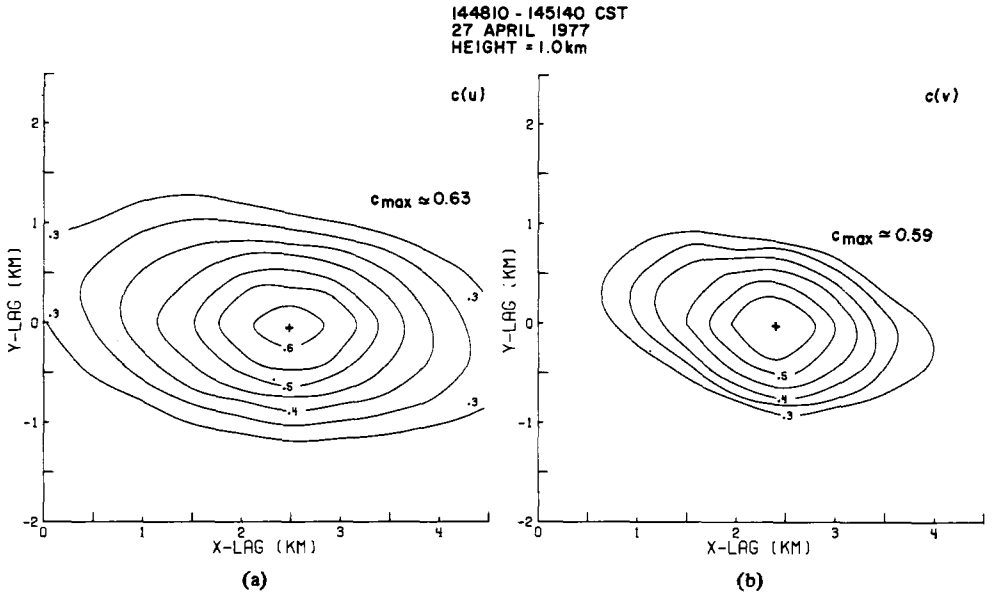

Fig. 36. Cross correlation coefficients c (as a function of horizontal spatial lag) of (a) the u component (in the direction of mean wind) for two wind fields, at 1.0 km AGL, synthesized 3½ min apart. The mean wind speed is 14.9 m·s^{-1} and the medium times for the two fields are 1448:10 CST and 1451:40 CST (b) the v component (transverse to the mean wind). A spatial lag corresponding to mean wind advection during the 3½ min time interval maximizes both $c(u)$ and $c(v)$.

analyzed aircraft gust probe data collected on this day during the time of the radar observation. They also detect a prominent peak in power density at a wavelength of about 4 km in the y direction.

4) Time Correlation of Clear Air Wind Perturbations: The cross correlated (in space and time) wind fields (synthesized 3-1/2 min apart) at 1.0 km above ground level (AGL) show that correlation is maximized for a translation equal to mean wind advection (Fig. 36) proving that these convective kinematic features advect with the mean wind. O'Bannon [92] has traced the time evolution of clear air eddies using wind synthesized from a sequence of dual Doppler-radar data acquired 30 s apart. His results demonstrate that clear air eddy fields of kilometer scales have a time scale of at least 10 min and, as with results on April 27, 1977, correlation is maximized when eddy winds are displaced to account for advection by the mean wind.

VII. Conclusions

The introduction of Doppler frequency shift measurement capability into weather radars has opened new horizons for exploration by atmospheric scientists. The astounding success achieved with these radars in detection of thunderstorm cyclones well in advance of tornado formation should cause incorporation of coherent systems in new radars used for operation by the national services. Advances in digital signal processing and display techniques have allowed economical development of real time presentation of the three principal Doppler spectral moments. The techniques are here and constantly improving, and we believe that important new scientific disclosures and new operational applications in the areas of wind measurement and tornado detection are forthcoming.

Doppler radars at centimeter wavelengths do not have a sufficiently large velocity-range ambiguity product $r_a v_a$ to match that required to observe, without obscuration, severe convective storms. There is no comprehensive data and documentation that show the full extent of the problem nor is there any foreseeable solution. Thus it appears that storm observers will have to accept some limitations in Doppler radar weather measurements.

Dual Doppler-radar observations of the kinematic structure of severe storms and the planetary boundary layer (PBL) agree with theoretical models but much investigation is still required. The Doppler weather radar shows promise of greatly increasing our knowledge of thunderstorms and the planetary boundary layer on scales not before possible. Furthermore, we can monitor significant mesoscale phenomena which are of importance to air traffic safety, air pollution control, and (perhaps most important) we may be able to see the triggering impulses of severe storms that each year cause such destruction. Increased power and sensitivity of weather radars may soon result in the meteorologist being able to observe the wind structure and its evolution throughout the troposphere.

The important advances in meteorological observations brought forth by the application of Doppler techniques to weather radars will continue in the future. However, there is room for further improvement in the radar system to reduce the deleterious effect of ambiguities while lessening data acquisition time for observation of severe storm convection, shear, and turbulence in clear or precipitation laden air.

Acknowledgment

The authors appreciate the support they have received from their colleagues in the Environmental Research Laboratories (ERL), Air Force Geophysics Laboratory, National Weather Service, Energy Research and Development Administration, National Research Council, and Federal Aviation Administration, not only in the preparation of this paper, but also for the continuing development of Doppler weather radar technology. We are particularly indebted to Dr. R. Strauch of the Wave Propagation Laboratory (ERL) and a reviewer whose careful study of this manuscript has significantly improved

the text. We are indebted to Ms. Joy Walton for her efficient and accurate typing and careful editing of the manuscript.

REFERENCES

[1] M. Abramowitz and I. A. Stegun, *Handbook of Mathematical Functions*, Nat. Bur. Standards, Appl. Math. Ser. 55, 2nd printing, Supp. Doc., U.S. Gov. Printing Office, Washington, DC, 1964.

[2] L. Armijo, "A theory for the determination of wind and precipitation velocities with Doppler radars," *J. Atmos. Sci.*, vol. 26, pp. 570-573, 1969.

[3] G. M. Armstrong and R. J. Donaldson, Jr., "Plan shear indicator for real time Doppler radar identification of hazardous storm winds," *J. Appl. Meteorol.*, vol. 8, pp. 376-383, 1969.

[4] D. Atlas, "Radar analysis of severe storms," *Meteorol. Monographs*, Amer. Meteorol. Soc., Boston, MA, 02108, vol. 5, no. 27, pp. 177-222, 1963.

[5] —, "Advances in radar meteorology," in *Advances in Geophysics*, Landsberg and Mieghem, Eds. New York: Academic, pp. 317-478, 1964.

[6] D. Atlas, K. R. Hardy, K. M. Glover, I. Katz, and T. G. Konrad, "Tropopause detected by radar," *Science*, vol. 153, pp. 1110-1112, 1966.

[7] D. Atlas, R. C. Srivastava, and R. S. Sekhon, "Doppler radar characteristics of precipitation at vertical incidence," *Rev. Geophys. Space Phys.* vol. 2, pp. 1-35, 1973.

[8] B. B. Balsley, "The use of sensitive coherent radars to examine atmospheric parameters in the height range 1-100 km," in *Preprints 18th Conf. Radar Meteorol.*, Amer. Meteorol. Soc., Boston, MA 02108, pp. 190-193, Mar. 1978.

[9] B. B. Balsley, N. Ciasnos, D. T. Farley, and M. J. Baron, "Winds derived from radar measurements in the arctic troposphere and stratosphere," *J. Appl. Meteorol.*, vol. 16, pp. 1235-1239, Nov. 1977.

[10] L. J. Battan, "Some observations of vertical velocities and precipitation sizes in a thunderstorm," *J. Appl. Meteorol.*, vol. 3, pp. 415-420, 1964.

[11] —, *Radar Observation of the Atmosphere.* Chicago, IL: Univ. Chicago Press, 1973.

[12] B. R. Bean and E. J. Dutton, *Radio Meteorology*, Nat. Bur. Standards, Monograph 92, Supp. Doc., U.S. Gov. Printing Office, Washington, DC 20402, 1966.

[13] M. I. Berger and R. J. Doviak, "Dual Doppler-radar observations of wind fields in a dry convective boundary layer," in *Preprints Fourth Symp. Meteorol. Observ. Instru.*, Denver, CO Amer. Meteorol. Soc., Boston, MA pp. 219-226, 1978.

[14] T. Berger and H. H. Groginsky, "Estimation of the spectral moments of pulse trains," *presented at the Int. Conf. Inform. Theory* (Tel-Aviv, Israel, 1973).

[15] L. V. Blake, "Prediction of radar range," in *Radar Handbook*, Merrill I. Skolnik, Ed. New York: McGraw-Hill, 1970, ch. 2.

[16] M. Born and E. Wolf, *Principles of Optics*, 2nd ed. New York: MacMillan, 1964.

[17] E. N. Boyenval, Echoes from precipitation using pulsed Doppler radar," in *Proc. 8th Weather Radar Conf.*, Amer. Meteorol. Soc., Boston, MA 02108, pp. 57-64, 1960.

[18] E. A. Brandes, "Optimizing rainfall estimates with the aid of radar," *J. Appl. Meteorol.*, vol. 14, pp. 1339-1345, 1975.

[19] J. Q. Brantley and D. A. Barczys, "Some weather observations with continuous wave Doppler radar," in *Proc. 6th Weather Radar Conf.*, Amer. Meteorol. Socl, Boston, MA. 02108, pp. 297-306, 1957.

[20] O. Brovko, "The structure of a maximum likelihood center frequency estimator," Tech. Internal Corresp. No. 2313.00/042, Hughes Aircraft Co., May 16, 1977.

[21] R. A. Brown, L. R. Lemon, and D. W. Burgess, "Tornado detection by pulsed Doppler-radar," *Mon. Weather Rev.*, vol. 106, no. 1, pp. 29-38, Jan. 1978.

[22] K. A. Browning and R. Wexler, "A determination of kinematic properties of a wind field using Doppler-radar," *J. Appl. Meteorol.*, vol. 7 no. 2, pp. 105-113, 1968.

[23] J. P. Burg, "Maximum entropy spectral analysis," *presented at the 37th Annu. Meeting Soc. Exploration Geophysicists* (Oklahoma City, OK, Oct. 1967).

[24] D. W. Burgess, "Single Doppler radar vortex recognition: Part I—Mesocyclone signatures," in *Preprints 17th Conf. Radar Meteorol.*, Amer. Meteorol. Soc., Boston, MA 02108, pp. 97-103, Oct. 1976.

[25] D. W. Burgess, J. D. Bonewitz, and D. R. Devore, "Joint Doppler operational project: Results year 1," in *Preprints 18th Conf. Radar Meteorol.*, Amer. Meteorol. Soc., Boston, MA 02108, pp. 442-448, Mar. 1978.

[26] D. W. Burgess, L. D. Hennington, R. J. Doviak, and P. S. Ray, "Multimoment Doppler display for severe storm identification," *J. Appl. Meteorol.*, vol. 15, pp. 1302-1306, 1976.

[27] W. C. Campbell and R. C. Strauch, "Meteorological Doppler radar with double pulse transmission," in *Preprints 17th Conf. Radar Meteor.*, Amer. Meteorol. Soc., Boston, MA 02108, pp. 42-44, Oct. 1976.

[28] P. A. F. Caton, "Wind measurement by Doppler radar," *Meteorol. Mag.*, vol. 92, pp. 213-222, 1963.

[29] R. B. Chadwick and G. R. Cooper, "Measurement of distributed targets with the random signal radar," *IEEE Trans. on Aerosp. Electron Syst.*, vol. AES-8, pp. 743-750, Nov. 1972.

[30] R. B. Chadwick, K. P. Moran, and G. E. Morrison, "Measurements toward a C_n^2 climatology, in *Preprints 18th Conf. Radar Meteorol.*, Amer. Meteorol. Soc., Boston, MA 02108, pp. 100-103, Mar. 1978.

[31] A. A. Chernikov, "Radio-wave scattering in clouds and the radar equation," in *Radar Meteorology: Proceedings of the Third All-Union Conf.* (1968), V. V. Kostarev, A. A. Chernikov, and A. B. Shupyatskii, Eds., translated by Don Hardin. Jerusalem, Israel: Keter, 1971.

[32] A. A. Chernikov, Yu. V. Mel'nichuk, N. Z. Pinus, S. M. Shmeter, and N. K. Vinnichenko, "Investigations of the turbulence in convective atmosphere using radar and aircraft," *Rad. Sci.*, vol. 4, no. 12, pp. 1257-1259, 1969.

[33] A. M. Chimera, "Meteorological radar echo study," Final Rep. Contract AF33(616)-6352, Cornell Aerosp. Labs., Buffalo, NY, 1960.

[34] J. W. Cooley and J. W. Tukey, "An algorithm for the machine calculation of complex Fourier series," *Math Comp.*, vol. 19, pp. 297-301, 1965.

[35] R. K. Crane, "Automatic cell detection and tracking," *Special Issue on Radio Meteorol., IEEE Trans. Geosci. Electron*, Oct 1979.

[36] —, "Stratospheric turbulence analysis," Final Rep AFGL-TR-0207, Air Force Geophys. Lab., Hanscom AFB, MA 01731, 1977.

[37] K. C. Crawford, "The design of a multivariate mesoscale field experiment," Ph.D. dissertation, Univ. of Oklahoma, Norman, OK 73069, 1977.

[38] W. B. Davenport and W. L. Root, *An Introduction to the Theory of Random Signals and Noise.* New York: McGraw-Hill, 1958.

[39] G. W. Deley, "Waveform design," in *Radar Handbook*, Merrill I. Skolnik, Ed. New York: McGraw-Hill, 1970, pp. 3-1-3-47.

[40] J. N. Denenberg, "The estimation of spectral moments," Rep. Lab. Atmos. Probing, Dep. Geophys. Sci., Univ. Chicago and Dep. Elec. Eng., Illinois Inst. Tech., 82 pp., 1971.

[41] R. J. Donaldson, Jr., "A demonstration of antenna beam errors in radar reflectivity patterns," *J. Appl. Meteorol.*, vol. 3, pp. 611-623, Oct. 1964.

[42] —, "Vortex signature recognition by a Doppler radar," *J. Appl. Meteorol.*, vol. 9, pp. 661-670, 1970.

[43] R. J. Doviak, J. Goldhirsh, and A. R. Miller, "Bistatic radar detection of high altitude clear-air atmospheric targets," *Rad. Sci.* vol. 7, pp. 993-1003, 1972.

[44] R. J. Doviak and D. Sirmans, "Doppler-radar with polarization diversity," *J. Atmos. Sci.*, vol. 30, pp. 737-738., 1973.

[45] R. J. Doviak, D. Burgess, L. Lemon, and D. Sirmans, "Doppler velocity and reflectivity structure observed within a tornadic storm," *J. Rech. Atmos.*, vol. VIII, nos. 1-2, pp. 235-243, Jan.-June 1974.

[46] R. J. Doviak, R. S. Ray, R. G. Strauch, and L. J. Miller, "Error estimation in wind fields derived from dual-Doppler radar measurement," *J. Appl. Meteorol.*, vol. 15, no. 8, pp. 868-878, 1976.

[47] R. J. Doviak and C. T. Jobson, "Dual Doppler-radar observations of clear air wind perturbations in the planetary boundary layer," *J. Geophys. Res.*, vol. 84, no. C2, pp. 697-702, 1979.

[48] R. J. Doviak, D. Sirmans, D. Zrnić, and G. B. Walker, "Considerations for pulse-Doppler radar observations of severe thunderstorms," *J. Appl. Meteorol.*, vol. 17, no. 2. pp. 189-205, 1978.

[49] R. J. Doviak and D. S. Zrnić, "Receiver bandwidth effect on reflectivity and Doppler velocity estimates," *J. Appl. Meteorol.*, vol. 18, no. 1, pp. 69-76, 1979.

[50] R. W. Fetter, "Real time analog Doppler processing (RANDOP)," in *Preprints 16th Conf. Radar Meteorol.*, Amer. Meteorol. Soc., Boston, MA, pp. 153-555, 1975.

[51] G. B. Foote and P. S. duToit, "Terminal velocity of raindrops aloft," *J. Appl. Meteorol.*, vol. 8, pp. 249-253, 1969.

[52] A. S. Frisch and S. F. Clifford, "A study of convection capped by a stable layer using Doppler radar and acoustic echo sounders," *J. Atmos. Sci.*, vol. 31, pp. 1622-1628, 1974.

[53] A. S. Frisch, L. J. Miller, and R. G. Strauch, "Three-dimensional air motion measured in snow," *Geophy. Res. Lett.*, vol. 1, pp. 86-89, 1974.

[54] K. S. Gage, W. P. Birkemeyer, and W. H. Jasperson, "Atmospheric stability measurement at tropopause altitudes using forward-scatter CW radar," *J. Appl. Meteorol.*, vol. 12, pp. 1205-1212, 1973.

[55] K. S. Gage and J. L. Green, "Evidence for specular reflection from monostatic VHF radar observations of the stratosphere," *Rad. Sci.*, vol. 13, no. 6, pp. 991-1001, Nov.-Dec. 1978.
[56] R. O. Gilmer, R. E. McGavin, and R. F. Reinking, "A small aircraft gust probe system for studies of boundary layer convection and transport," in *Preprints Fourth Symp. Meteorol. Observ. Instru.*, Amer. Meteorol. Soc., Boston, MA, pp. 426-432, Apr. 1978.
[57] E. E. Gossard, J. H. Richter, and D. R. Jensen, "Effect of wind shear on atmospheric wave instabilities revealed by FM-CW radar observations," in *Boundary-Layer Meteorology*, vol. 4. Dordrecht, The Netherlands: Reidel, 1973, pp. 113-131.
[58] E. E. Gossard and W. R. Moninger, "The influence of a capping inversion on the dynamic and convective instability of a boundary layer model with shear," *J. Atmos. Sci.*, vol. 32, pp. 2111-2124, 1975.
[59] E. E. Gossard and A. S. Frish, "Kinematic models of a dry convective boundary layer compared with dual Doppler-radar observations of wind fields," in *Boundary-Layer Meteorology*, vol. 10. Dordrecht, The Netherlands: Reidel, 1976, pp. 311-330.
[60] J. L. Green, J. M. Warnock, R. H. Winkler, and T. E. VanZandt, "Studies of winds in the upper troposhere with a sensitive VHF radar," *Geophys. Res. Letts.*, vol. 2, pp. 19-21, Jan. 1975.
[61] J. L. Green, R. H. Winkler, J. M. Warnock, W. L. Clark, K. S. Gage, and T. E. VanZandt, "Observations of enhanced clear air reflectivity associated with convective clouds," in *Preprints 18th Conf. Radar Meteorol.*, Amer. Meteorol. Soc., Boston, MA, pp. 88-93, Mar. 1978.
[62] H. L. Groginsky, "The coherent memory filter," *Electron Prog.*, Raytheon Co., vol. 9, no. 3. pp. 7-13, 1965.
[63] K. R. Hardy, D. Atlas, and K. M. Glover, "Multiwavelength backscatter from the clear atmosphere," *J. Geophys. Res.*, vol. 71, no. 6, pp. 1537-1552, 1966.
[64] K. R. Hardy and I. Katz, "Probing the clear atmosphere with high power, high resolution radars," *Proc. IEEE*, vol. 57, pp. 468-480, 1969.
[65] T. W. Harrold and K. A. Browning, "Identification of preferred areas of shower development by means of high power radar," *Quart. J. Roy. Meteorol. Soc.*, vol. 97, no 413, pp. 330-339, July 1971.
[66] C. W. Helstrom, *Statistical Theory of Signal Detection*. New York: Pergamon, 1968.
[67] L. Hennington, R. J. Doviak, D. Sirmans, D. Zrnić, and R. G. Strauch, "Measurements of winds in the optically clear air with microwave pulse-Doppler radar," in *Preprints 17th Conf. Radar Meteorol.*, Amer. Meterol. Soc., Boston, MA, pp. 342-348, Oct. 1976.
[68] S. L. Hess, *Introduction to Theoretical Meteorology*. New York: Holt, Rinehart, and Winston, 1959.
[69] J. J. Hicks and J. K. Angell, "Radar observations of breaking gravitational waves in the visually clear atmosphere," *J. Appl. Meteorol.*, vol. 7, pp. 114-121, Feb. 1968.
[70] W. Hitschfeld and A. S. Dennis, "Turbulence in snow generating cells," *Sci. Rep. MW-23*, McGill Univ., Montreal, p-Q., Canada, 31 pp., 1956.
[71] E. M. Hofstetter, "Simple estimates of wake velocity parameters," M.I.T. Lincoln Lab., Lexington, MA, unpublished Tech. Note 1970-11, 1970.
[72] G. H. Hyde and K. E. Perry, "Doppler phase difference integrator," M.I.T. Tech. Rep. 189, 1958.
[73] I. Katz, "Sea breeze structure as seen by radar," Appl. Phys. Lab., Johns Hopkins Univ. Memo BPD 66U-25, 1966.
[74] T. G. Konrad, "The alignment of clear air convective cells," *Proc. Intern Conf. Cloud Phys.*, Toronto, Ont., Canada, pp. 539-543, 1968.
[75] —, "The dynamics of the convective process in the clear air as seen by radar," in *Preprints 14th Conf. Radar Meteorol.*, Amer. Meteorol. Soc., Boston, MA, pp. 57-60, 1970.
[76] R. A. Kropfli and N. M. Kohn, "Persistent horizontal rolls in the urban mixed layer as revealed by dual-Doppler radar," *J. Appl. Meteorol.*, vol. 17, pp. 669-676, May 1978.
[77] J. P. Kuettner, "Cloud bands in the earth's atmosphere," *Tellus XXIII*, vol. 4-5, pp. 404-425, 1971.
[78] J. T. Lee, "Application of Doppler weather radar to turbulence measurements which affect aircraft," *Final Rep.* #FAA-RD-77-145, Syst. Res. Development Serv., FAA, Washington, DC 20590, 1977.
[79] J. T. Lee and C. Goff, "Gust front wind shear and turbulence—concurrent aircraft and surface based observations," in *Preprints 7th Conf. Aerosp. Aeronaut. Meteorol. Symp. Remote Sensing from Satellites*, Melbourne, FL, Amer. Meteorol. Soc., Boston, MA, pp. 48-54. 1976.
[80] R. M. Lhermitte, "Motions of scatterers and the variance of the mean intensity of weather radar signals," Sperry-Rand Research Center, 5RRC-RR-63-57, Sudbury, MA, 1963.
[81] —, "Doppler radars as severe storm sensors," *Bull. Amer. Meteorol. Soc.*, vol 45, pp. 587-596, 1964.
[82] —, "Dual-Doppler radar observations of convective storm circulation," in *Preprints 14th Conf. Radar Meteorol.*, Amer. Meteorol. Soc., Boston, MA, pp. 153-156, 1970.
[83] —, "Real time processing of meteorological Doppler radar signals, in *Preprints 15th Conf. Radar Meteorol.*, Amer. Meteorol. Soc., Boston, MA, pp. 364-367, 1972.
[84] R. M. Lhermitte and D. Atlas, "Precipitation motion by pulse Doppler radar," in *Proc. 9th Conf. Weather Radar*, Amer. Meteorol. Soc., Boston, MA, pp. 218-223, 1961.
[85] J. S. Marshall and W. Hitschfeld, "Interpretation of the fluctuating echo from randomly distributed scatterers," *Can. J. Phys.*, vol. 31, pt. I, pp. 962-995, 1953.
[86] J. H. Meyer, "Radar observations of iand breeze fronts at Wallops Island, Virginia," in *Preprints 14th Conf. Radar Meteor.*, Amer. Meteorol., Soc., Boston, MA, pp. 61-67, Nov. 1970.
[87] K. S. Miller and M. M. Rochwarger, "A covariance approach to spectral moment estimation," *IEEE Trans. Inform, Theory*, vol. IT-18, pp. 588-596, 1972.
[88] E. A. Mueller and E. J. Silha, "Unique features of the CHILL radar system," in *Preprints 18th Conf. Radar Meteorol.*, Amer. Meteorol. Soc., Boston, MA, pp. 381-382, Mar. 1978.
[89] F. E. Nathanson, *Radar Design Principles*. New York: McGraw-Hill, 1969.
[90] F. E. Nathanson and P. L. Smith, "A modified coefficient for the weather radar equation," in *Preprints 15th Conf. Radar Meteorol.*, Amer. Meteorol. Soc., Boston, MA, pp. 228-230, Oct. 1972.
[91] L. R. Novick and K. M. Glover, "Spectral mean variance estimation via pulse pair processing," in *Preprints 16th Conf. Radar Meteorol.*, Amer. Meteorol. Soc., Boston, MA, pp. 1-5, 1975.
[92] T. O'Bannon, "A study of dual-Doppler synthesized clear air wind fields," in *Preprints 18th Conf. Radar Meteorol.*, Amer. Meteorol. Soc., Boston, MA, pp. 65-69, 1978.
[93] G. R. Ochs and R. S. Lawrence, "Temperature and C_n^2 profiles measured over land and ocean to 3 km above the surface," *NOAA Tech. Rep. ERL 251-WPL 22*, Boulder, CO, 39 pp., 1972.
[94] A. Papoulis, *Probability, Random Variables, and Stochastic Processes*. New York: McGraw-Hill, 1965.
[95] J. R. Probert-Jones, "The radar equation in meteorology," *Quart. J. Roy. Meteorol. Soc.*, vol. 88, pp. 485-495, 1962.
[96] J. R. Probert-Jones and W. G. Harper, "Vertical air motion in showers as revealed by Doppler radar," in *Proc. 9th Weather Radar Conf.*, Amer Meteorol. Soc., Boston, MA, pp. 225-232, 1961.
[97] P. S. Ray, R. J. Doviak, G. B. Walker, D. Sirmans, J. Carter, and B. Bumgarner, "Dual-Doppler observation of a tornadic storm," *J. Appl. Meteorol.*, vol. 14, no. 8, p. 1521-1530, 1975.
[98] P. L. Rice, A. G. Langley, K. A. Norton, and A. P. Barsis, "Transmission loss predictions for tropospheric communication circuits," Nat. Bur. Standards Tech. Note 101, vols. 1-2, Supp. Doc., U.S. Gov. Printing Office, Washington, DC 20402, 1967.
[99] J. H. Richter, "High resolution troposheric radar sounding, "Rad. Sci., vol. 4, pp. 1261-1268, 1969.
[100] R. R. Rogers, "The effect of variable target reflectivity on weather radar measurements," *Quart. J. Roy. Meteorol. Soc.*, vol. 97, pp. 154-167, 1971.
[101] J. Röttger and C. H. Liu, "Partial reflection and scattering of VHF radar signals from the clear atmosphere," *Geophys. Res. Lett.*, vol. 5, no. 5, pp. 357-360, May 1978.
[102] W. D. Rummler, "Introduction of a new estimator for velocity spectral parameters," Tech. Memo MM-68-4121-5, Bell Telephone Labs., Whippany, NJ, 1968.
[103] —, "Accuracy of spectral width estimators using pulse pair waveforms," Tech. Memo, Bell Telephone Labs., Whippany, NJ, 1968.
[104] W. Rutkowski and A. Fleisher, "R-meter: An instrument for measuring gustiness," *MIT Weather Radar Res. Rep. No. 24*, 1955.
[105] *Advances in Radio Research*, J. A. Saxton, Ed. vol. 1. New York: Academic, 226 pp., 1964.
[106] A. J. F. Siegert and H. Goldstein, *Propagation of Short Radio Waves*, D. E. Kerr, Ed., vol. 13, MIT Rad. Lab. Series, 1964, Appendix B.
[107] D. Sirmans and R. J. Doviak, "Meteorological radar signal intensity estimation," NOAA Tech. Memo ERL NSSL-64, 1973.
[108] —, "Pulsed-Doppler velocity isotach displays of storm winds in real time," *J. Appl. Meteorol.*, vol. 12, no. 4, pp. 694-697, 1973.
[109] D. Sirmans and B. Bumgarner, "Numerical comparison of five mean frequency estimators," *J. Appl. Meteorol.*, vol. 14, pp. 991-1003, 1975.
[110] —, "Estimation of spectral density mean and variance by covariance argument techniques," in *Preprints 16th Conf. Radar*

Meteorol., Amer. Meteorol. Soc., Boston, MA, pp. 6-13, Apr. 1975.
[111] D. Sirmans, D. Zrnić, and B. Bumgarner, "Estimation of maximum unambiguous Doppler velocity by use of two sampling rates," in *Preprints 17th Conf. Radar Meteorol.*, Amer. Meteorol. Soc., Boston, MA, pp. 23-28, 1976.
[112] R. L. Smith and D. W. Holmes, "Use of Doppler radar in meteorological observations," *Monthly Weather Rev.*, vol. 89, pp. 1-7, 1961.
[113] P. L. Smith, Jr., K. R. Hardy, and K. M. Glover, "Applications of radar to meteorological operations and research," *Proc. IEEE*, vol. 62, pp. 724-745, June 1974.
[114] J. D. Stackpole, "The effectiveness of raindrops as turbulence sensors," in *Proc. 9th Weather Radar Conf.*, Amer. Meteorol. Soc., Boston, MA, pp. 212-217, 1961.
[115] R. G. Strauch, W. C. Campbell, R. B. Chadwick, and K. P. Moran, "FM-CW boundary layer radar with Doppler capability," NOAA Tech. Rep. ERL 329-WPL 39, Boulder, CO, 1975.
[116] R. G. Strauch and A. S. Frisch, "Doppler radar measurements of turbulent kinetic energy dissipation rates in a northeastern Colorado storm," *J. Appl. Meteorol.*, vol. 15, pp. 1012-1017, 1976.
[117] J. Sychra, "Relation between real and pulse volume averaged fields of reflectivity and velocity," *Canadian Meteorol. Service Res. Reps.*, 1972.
[118] V. I. Tatarski, *Wave Propagation in a Turbulent Medium* (translation by R. A. Silverman). New York: McGraw-Hill, 1961.
[119] J. W. Taylor and J. Mattern, "Receivers," Radar Handbook, Merrill I. Skolnik, Ed. New York: McGraw-Hill Book Co., 1970, Ch. 5.
[120] C. W. Ulbrich and D. Atlas, "The rain parameter diagram: Methods and applications," *J. Geophys. Res.*, vol. 83, no C3, pp. 1319-1325, 1978.
[121] T. E. VanZandt, J. L. Green, D. S. Gage, and W. L. Clark, "Vertical profiles of refractivity turbulence structure constant: Comparison of observations by the sunset radar with new theoretical model," *Rad. Sci.*, vol. 13, pp. 819-829, 1978.
[122] P. Waldteufel, "An analysis of weather spectra variance in a tornadic storm," NOAA Tech. Memo ERL NSSL-76, 1976.
[123] R. F. Woodman and T. Hagfors, "Methods for the measurement of vertical ionospheric motions near the magnetic equator by incoherent scattering," *J. Geophys. Res. Space Phys.*, vol. 75, pp. 1205-1212, Mar. 1969.
[124] R. F. Woodman and A. Guillen, "Radar observations of winds and turbulence in the stratosphere and mesosphere," *J. Atmos. Sci.*, vol. 31, pp. 493-505, 1974.
[125] A. M. Yaglom, "On the local structure of the temperature field in a turbulent flow," *Dokl. Akad. Nauk SSSR*, vol. 69, p. 743, 1949.
[126] G. W. Zeoli, "If versus video limiting for two-channel coherent signal processors," *IEEE Trans. Inform. Theory*, vol. IT-17, pp. 579-587, Sept. 1971.
[127] D. Zrnić, "Moments of estimated input power for finite sample averages of radar receiver outputs," *IEEE Trans. Aerosp. Electron. Syst.*, vol. AES-11, pp. 109-113, 1975.
[128] —, "Estimated tornado spectra and maximum velocity statistics," Final Rep. Grant No. 04-5-022-17, 1975.
[129] —, "Signal-to-noise ratio in the output of nonlinear devices," *IEEE Trans. Inform. Theory*, vol. IT-21, pp. 662-663, Nov. 1975.
[130] —, "Spectral moment estimates from correlated pulse pairs," *IEEE Trans. Aerosp. Electron. Syst.*, vol. AES-13, pp. 344-354, 1977.
[131] D. Zrnić and B. Bumgarner, "Receiver chain and signal processing effects on the Doppler spectrum," in *Preprints 16th Conf. Radar Meteorol.*, Amer. Meteorol. Soc., Boston, MA, pp. 163-168, Apr. 1975.
[132] D. Zrnić and R. J. Doviak, "Velocity spectra of vortices scanned with a pulse-Doppler radar," *J. Appl. Meteorol.*, vol. 14, pp. 1531-1539, 1975.
[133] D. Zrnić, R. J. Doviak, and D. W. Burgess, "Probing tornadoes with pulse-Doppler radar," *Quart. J. Roy. Meteorol. Soc.*, vol. 103, vol 438, pp. 707-720, 1977.
[134] D. Zrnić and R. J. Doviak, "Matched filter criteria and range weighting for weather radar," *IEEE Trans. Aerosp. Electron. Syst.*, vol. AES-14, pp. 925-930, 1978.

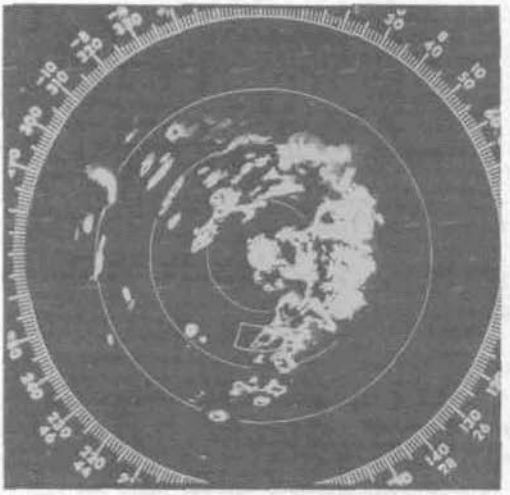

Fig. 15. WSR-57 PPI display of thunderstorm cells on a tornadic day (181704 CST April 19, 1976). Gray shadings (dim, bright, black, dim, etc.) represent dBZ levels differing by about 10 dBZ starting at 17 dBZ. Range marks are 100 km apart, elevation angle = 0.0°. Unambiguous range is 910 km. The boxed area outlines a tornadic storm cell whose mesocyclone signature was detected in real time by NSSL's Norman (NOR) Doppler radar which is nearly colocated with the WSR-57.

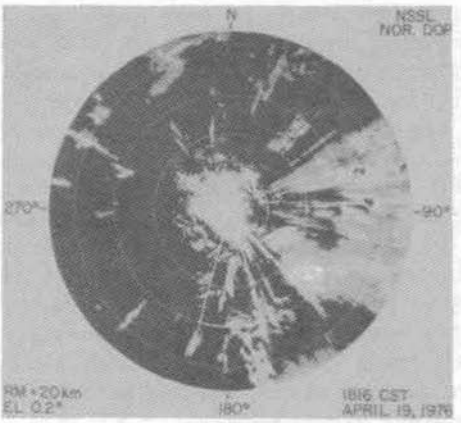

Fig. 16. Same storm system (181635 CST) seen with the Doppler radar having 115-km unambiguous range. 10-log Z brightness categories (dim, bright . . .) start at 10 dBZ and increment at about 10-dBZ steps. The 10-log Z scale applies only to first-trip echoes. Some range-overlaid echoes can be recognized by their radially elongated shape. The box outlines the same area as in Fig. 15. Range marks are 20 km apart. Part of the tornadic storm is obscured by a nearby (30–60-km range) storm.

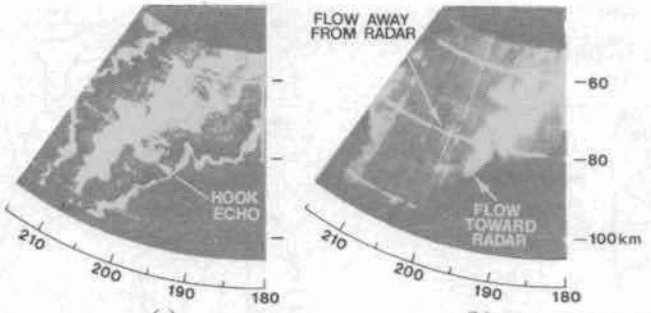

Fig. 26. Storm reflectivity (a) and isodops (b) displayed on PPI at 2115 CST. The elevation angle is 1.9°, range marks correspond to 60, 80, 100 km. Reflectivity factor categories are: dim (<21 dBZ), bright (21–31), black (31–44), dim (44–57), and bright (>57 dBZ). Velocity categories are dim <13 ms^{-1}), bright (13–21), and brightest (>21). Positive radial velocities are angularly strobed in brightness. Mesocyclone signature is between 194°–203° and 73–90 km.

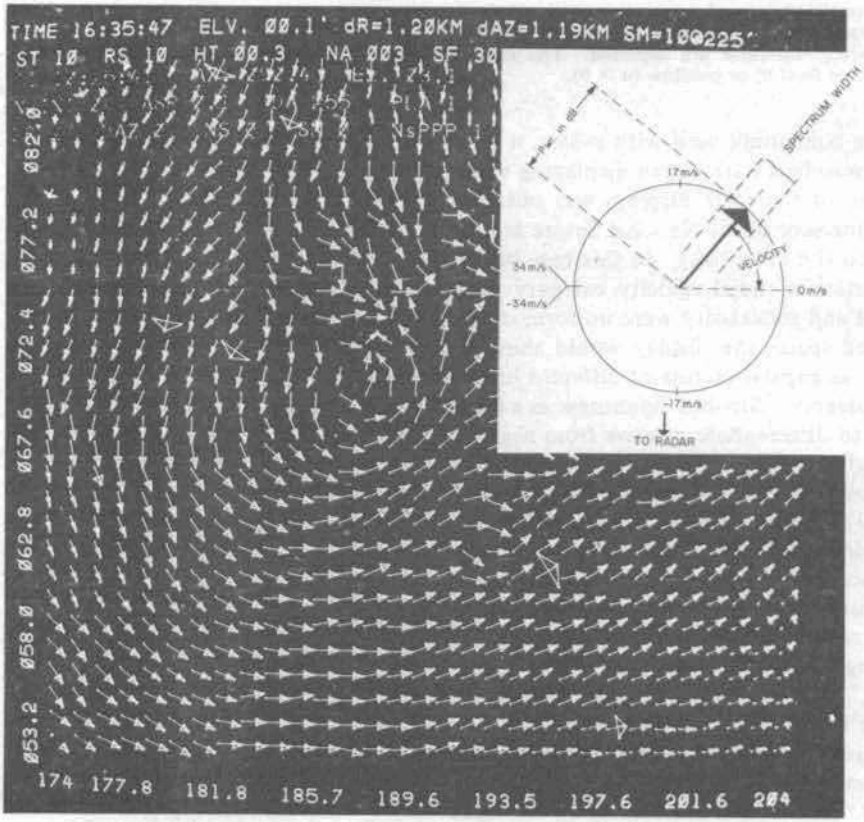

Fig. 27. The multimoment Doppler display of a mesocyclone. Each arrow contains information of the 3 principal Doppler spectrum moments for a resolution volume. For interpretation of arrows see insert in upper right corner (arrow length is proportional to received power, arrow direction to velocity and arrowhead size to Doppler spectrum width). Abscissa is azimuth and ordinate scale denotes range (km) from radar. Housekeeping information is at top of screen.

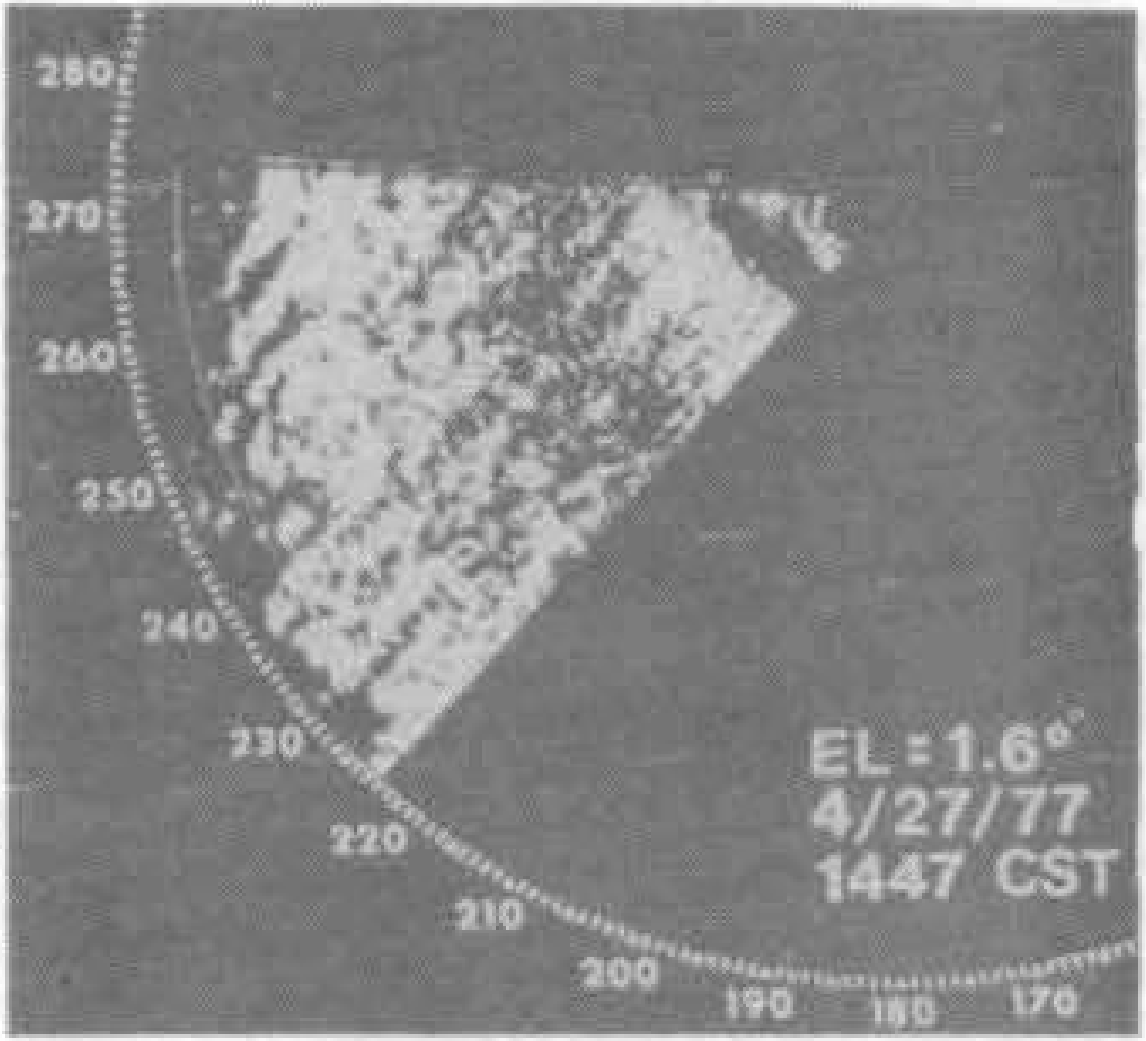

Fig. 31. PPI sector scan of echo power from clear air seen by the NRO Doppler radar. Bright area of high power is aligned roughly parallel to mean wind and bands are spaced about 4 km apart. Range marks are 20 km apart. EL = 1.6° (April 27, 1977, 1447 CST).